
Weather-Robust Cross-View Geo-Localization via Prototype-Based Semantic Part Discovery

Chi-Nguyen Tran^{1,†}

23122044@student.hcmus.edu.vn

Dao Sy Duy Minh^{1,†}

23122041@student.hcmus.edu.vn

Huynh Trung Kiet^{1,†}

23122039@student.hcmus.edu.vn

Nguyen Lam Phu Quy¹

23122048@student.hcmus.edu.vn

Phu-Hoa Pham¹

23122030@student.hcmus.edu.vn

Long Tran-Thanh^{2,*}

long.tran-thanh@warwick.ac.uk

Abstract

Low-altitude economy has been experiencing rapid growth in recent years, with significant contributions to the global economy. While common drone tasks such as delivery, inspection, and search-and-rescue typically use Global Navigation Satellite Systems (GNSS) to navigate, there is an increasing need for developing alternative solutions as GNSS signals can be easily jammed, spoofed, or unavailable over a prolonged operational time. As such, cross-view geo-localization (CVGL), which matches an oblique drone view to a geo-referenced satellite tile, has emerged as a potent alternative that lets an autonomous drone localize itself when GNSS fails. Despite strong recent progress, three limitations persist in current CVGL methods: 1) global-descriptor designs compress the patch grid into a single vector without separating what is shared across the view gap (layout) from what is not (texture); 2) altitude-related scale variation is implicitly retained in the learned embedding rather than treated as a nuisance to be marginalized out; and 3) multi-objective training relies on hand-tuned scalars over losses that live on incompatible gradient scales. To address these limitations, we propose SKYPART, a lightweight swappable head for patch-based vision transformers (ViTs) that institutes explicit part grouping over the patch grid. SKYPART has four components grounded in established theory: (i) learnable prototypes that compete for patch tokens via a single-pass cosine assignment; (ii) altitude-conditioned linear modulation applied only during training so that the retrieval embedding is altitude-free at inference; (iii) a graph-attention readout over active prototypes, and (iv) a Kendall uncertainty-weighted multi-objective loss whose stationary points are Pareto-stationary. At 26.95 M parameters and 22.14 GFLOPs, SKYPART is the smallest among the top-performing methods in our comparison and sets a new state of the art on SUES-200, University-1652, and DenseUAV datasets under a single-pass, no-re-ranking, no test-time augmentation (TTA) protocol. Furthermore, its accuracy gap to the strongest baseline widens under the ten-condition WeatherPrompt corruption benchmark.

¹Faculty of Information Technology, University of Science, Vietnam National University, Ho Chi Minh City, Vietnam.

²Department of Computer Science, University of Warwick, Coventry, United Kingdom.

[†]Equal contribution. *Corresponding author.

1 Introduction

Autonomous drones and autonomous driving are two of the fastest maturing AI application areas in the last five years. Both are moving from research demonstration to large-scale deployment-commercial drone delivery and inspection fleets, and self-driving vehicle pilots in dozens of cities. Both domains share the same hard requirement: the agent must know where it is on a prior map, in real time, without relying on a radio signal that an adversary or a dense urban canyon can take away. This requires efficient robust visual geo-localization against a previously captured overhead map, which has drawn increasing attention from the research community. In particular, an autonomous drone that cannot localize itself cannot complete a mission. Global Navigation Satellite System (GNSS) jamming and spoofing are now routine in contested airspace and dense urban canyons [Radoš et al., 2024, Couturier and Akhlofi, 2021], and the next generation of low-altitude services, such as last-mile delivery, precision agriculture, search-and-rescue swarms, and infrastructure inspection, is being designed on the premise that radio signals may be absent or adversarial. Cross-view geo-localization (CVGL), which matches an oblique drone image to a geo-referenced satellite tile, has become one of the most important techniques to address this challenge, as it has the potential to remain robust under altitude change, weather corruption, and tight onboard compute budgets, requirements that are typical of many modern-day visual navigation tasks.

The core difficulty of CVGL is that the visual statistics that modern recognition techniques rely on (e.g., texture, colour, local contrast) are precisely the statistics that change most frequently between views and under weather. This leads to three limitations that persist in the current CVGL literature: 1) global-descriptor designs [Wu et al., 2024, Deuser et al., 2023, Du et al., 2024] compress the patch grid into a single vector with no mechanism to separate what is shared across the view gap from what is not; 2) altitude-related scale variation is implicitly retained in the learned embedding rather than marginalized as a nuisance; and 3) multi-objective training relies on hand-tuned scalars over losses on incompatible gradient scales.

We argue that to address these issues, one needs to factor out texture and keep the spatial organization of recurring components such as roads, roofs, and vegetation patches. We hypothesize that layout cues are more stable than texture under viewpoint, lighting, and sensor changes, and build SKYPART around that assumption [Marr and Nishihara, 1978, Biederman, 1987]. Following the invariance vs. sufficiency trade-off of the information bottleneck [Achille and Soatto, 2018], we adopt the working assumption that a good retrieval embedding should approximate the minimal sufficient statistic of the geolocation signal after nuisance variables have been marginalized out. Given this, our idea is that CVGL should be formulated around explicit grouping rather than ever-larger global pooling, where self-supervised ViTs can be used to expose emergent object-centric structure at the patch level [Caron et al., 2021, Oquab et al., 2024], and object-centric learning to identify a small set of competing slots to carve that structure into discrete, reusable components [Locatello et al., 2020]. The layout of those components is what is shared across the drone/satellite gap.

This idea reformulates the aerial CVGL problem as a layout-centric factorization problem, from which four architectural choices follow directly: prototype-based part discovery, nuisance-aware training modulation, multi-objective training, and active prototypes identification. To implement this pipeline, we develop SKYPART, which consists of:

1. Single-pass cosine assignment module for prototype-based part discovery [Locatello et al., 2020, Luo et al., 2023, Sun et al., 2018];
2. Altitude-conditioned Feature-wise Linear Modulation (FiLM) [Perez et al., 2018, Dumoulin et al., 2018], which is applied only during training, so altitude is a nuisance to marginalize rather than an inference feature;
3. Kendall-weighted multi-objective loss optimizer [Kendall et al., 2018] over four heads (alignment, part quality, altitude, distillation) whose stationary points are Pareto-stationary [Sener and Koltun, 2018];
4. A graph-attention readout [Veličković et al., 2018, Kipf and Welling, 2017] over active prototypes, which carries the pairwise compatibility of discovered components alongside the global image representation derived from the classification token (CLS) of the ViT.

We also apply a lightweight swappable head for patch-based ViTs that operationalizes the reformulation and trains end-to-end with a new loss function called GEOPARTLOSS. As such, the inference pipeline of SKYPART is a single forward pass with cosine similarity, no re-ranking, no test-time aug-

mentation, and no query expansion. Note that SKYPART ranks first on SUES-200, University-1652, and DenseUAV under our evaluation protocol (single-pass, no-re-ranking, no-TTA; see Sec. 4.2), and is the most parameter-efficient among the top-accuracy-tier methods in the comparison. Under the reported WeatherPrompt protocol [Wen et al., 2025], SKYPART shows the strongest mean robustness, with especially large gains under fog+snow and darkness; SUES-200 and University-1652 baselines are taken from their published configurations and SKYPART is evaluated under a shared corruption pipeline, so resolution and training-budget differences (detailed in Sec. 4.4) are reported explicitly rather than fully resolution-controlled. Overall, SKYPART is among the most parameter- and compute-efficient methods in the top-accuracy tier (26.95 M, 22.14 GFLOPs), retains a strong relative robustness margin under the WeatherPrompt [Wen et al., 2025] corruption benchmark, and we further include a lessons-learned catalogue of the methods we tried that underperformed (Appendix A4.3).

We also apply SKYPART to the problem of zero-shot cross-dataset transfer (University-1652 \rightarrow SUES-200). Here, SKYPART leads all Drone \rightarrow Satellite cells and remains competitive on Satellite \rightarrow Drone, where dedicated baselines retain advantages in some R@1/AP cells (see Appendix A3.5 for the full table).

2 Related Work

Cross-View Geo-Localization. CVGL began as a ground \rightarrow aerial retrieval problem [Workman et al., 2015, Lin et al., 2015, Hu et al., 2018], solved by NetVLAD-style aggregators [Arandjelović et al., 2016] and triplet objectives [Schroff et al., 2015], and sharpened by geometry-aware priors such as polar warping [Shi et al., 2020]. The UAV benchmarks [Zheng et al., 2020, Zhu et al., 2023, Dai et al., 2024] removed most of that prior because a drone’s oblique angle and continuous altitude variation replace a clean radial warp with a soft projective distortion. Recent UAV CVGL has responded on two fronts: a scale-up line stacking larger ConvNeXt-B backbones with hard-negative sampling and attention-based partitioning [Dai et al., 2022, Shen et al., 2024, Deuser et al., 2023, Chen et al., 2024, Du et al., 2024, Wu et al., 2024, Chen et al., 2025, Hou et al., 2025], and an efficiency line that shrinks the model at a cost in accuracy [Wang et al., 2022, Liu et al., 2024, Xu et al., 2025a, Ping et al., 2025, Gao et al., 2025, Sun et al., 2024]. Both lines retain a global-descriptor commitment, sometimes augmented by a fixed spatial partition; partial-overlap settings [Ye et al., 2026] expose the low-altitude limit of both. SKYPART departs from this commitment and replaces the global pool with an explicit prototype grouping that the retrieval objective can reward directly. Closest in spirit among graph-based efficiency methods, SeGCN [Liu et al., 2024] relies on semantic categories from an auxiliary module to define graph nodes, while SKYPART discovers its prototype nodes end-to-end from patch-token competition without auxiliary semantic supervision.

Part-based Representations and Object-Centric Grouping. Part-based recognition has a long cognitive-vision history [Marr and Nishihara, 1978, Biederman, 1987, Sun et al., 2018], and its modern incarnation is slot attention [Locatello et al., 2020]: a small set of latents competes for input tokens through iterative attention, producing object-centric groupings without supervision. SegCLIP [Luo et al., 2023] projects this onto ViT patch tokens [Dosovitskiy et al., 2021, Vaswani et al., 2017] for open-vocabulary segmentation, and masked autoencoders and feature-masking variants [He et al., 2022, Zhou et al., 2022, Baevski et al., 2022] pursue analogous grouping through reconstruction. None was designed for cross-view retrieval, and the altitude nuisance specific to aerial imagery has no analogue in their benchmarks. SKYPART uses a single-pass cosine assignment (a fixed-point view of slot iteration that is sufficient when the downstream objective is retrieval rather than reconstruction), applies masking and distillation at the *part* level rather than the patch level so that reconstruction pressure targets layout rather than texture, and conditions the clustering pathway on altitude via FiLM [Perez et al., 2018, Dumoulin et al., 2018].

Metric Learning and Multi-Task Optimization. Our retrieval objective groups Circle [Sun et al., 2020], proxy-anchor [Kim et al., 2020], InfoNCE [van den Oord et al., 2018], and patch-level NCE into a single *alignment* task, and combines that alignment task with three further tasks-part quality, altitude regression, and distillation-via Kendall homoscedastic uncertainty weighting [Kendall et al., 2018], read through the alignment/uniformity decomposition of contrastive learning [Wang and Isola, 2020, Chen et al., 2020]: the decomposition predicts that alignment carries the signal and uniformity regularizes it, which the ablation in Sec. 4.5 confirms. The general theorem of Sener & Koltun [Sener and Koltun, 2018] guarantees that any positive-weighted scalarization of the four task losses is Pareto-stationary in the vector objective, and Kendall weighting produces such positive weights $\exp(-s_g)$ automatically; what it buys us over a hand-tuned scalar combination (which is also Pareto-stationary) is that the four weights are learned end-to-end rather than swept manually. The

relational readout over prototype nodes [Veličković et al., 2018, Kipf and Welling, 2017] complements the global CLS pathway; denoising [Feng et al., 2024] and domain-adversarial [Ganin and Lempitsky, 2015] alternatives are orthogonal. Distillation [Hinton et al., 2015, Gou et al., 2021, Tian et al., 2020, Ma et al., 2024, Park et al., 2019] is used only to stabilize the teacher-space projector during training, so the deployed pipeline has no external detector, diffusion front-end, or inference-time adaptation.

3 Method: SKYPART

3.1 Architecture Overview

We start with the shape of the head which follows from the framing we described in Sec. 1. If layout is the invariant we want the embedding to preserve across the drone/satellite gap, then the representation should expose an identity axis (what the recurring components are) and an arrangement axis (how they are spatially related), and it should do so without letting altitude, which is a nuisance observed at training but unreliable at test, leak into the retrieval embedding. Four choices fall out of this framing. First, the part branch is built as a competition between a small bank of prototypes for a larger set of patch tokens, with the softmax running over prototype indices rather than patch positions, so that each patch commits to a prototype rather than each prototype averaging over all patches. This is the single-pass analogue of slot attention [Locatello et al., 2020], which we treat as sufficient in our retrieval setting because the downstream objective does not require a reconstruction from the grouping. Second, a graph readout over the active prototype nodes can produce a separate arrangement embedding, complementing the identity-heavy part descriptor and the global CLS pathway, which refers to the branch that uses the CLS token as a global image descriptor¹. Third, altitude conditions the clustering pathway through a feature-wise affine modulation [Perez et al., 2018, Dumoulin et al., 2018] but is marginalized at inference through mean FiLM parameters. This yields an exact equivalence only at the modulation-operator level (linearity in γ, β), not a claim that training-conditioned features are globally unchanged (formal statement in Appendix A1.2). Fourth, the four training heads (alignment, part quality, altitude, and distillation) live on incompatible gradient scales. To combine them we use Kendall homoscedastic uncertainty weighting [Kendall et al., 2018]. Sener & Koltun’s general theorem [Sener and Koltun, 2018] guarantees Pareto-stationarity for any positive-weighted scalarization of the four task losses; Kendall weighting produces such positive weights $\exp(-s_g)$ automatically, so its advantage over a hand-tuned scalar combination (which is also Pareto-stationary) is that the four weights are learned end-to-end rather than swept manually. The theoretical justification of this idea can be found in Appendix A1.2.

Figure 1 depicts the resulting full pipeline. A shared patch-based encoder, DINOv2 ViT-S/14 in our experiments, chosen because its self-distillation pretext produces patch tokens with emergent object-centric structure [Caron et al., 2021, Oquab et al., 2024] that the prototype assignment can cluster on, processes both views to produce a CLS token and a set of patch tokens. The three branches read from these tokens: a global branch that keeps the CLS, a part branch that runs prototype competition and returns a part-pooled descriptor, and a graph branch that runs a two-layer Graph Attention Network (GAT) [Veličković et al., 2018] over per-view active prototype nodes (fully connected within each view; no explicit drone-satellite edges in the graph). A lightweight fusion gate combines the three into a single 768-D retrieval vector. Altitude-FiLM acts only as a metadata-conditioned branch during training; at inference it uses fixed mean FiLM parameters and requires no altitude input. The auxiliary signals (masked part reconstruction, teacher distillation, EMA self-ensembling) are discarded at inference. The deployed model is the student backbone plus the head, with cosine similarity and no re-ranking or test-time augmentation.

3.2 Semantic Part Discovery and Three-Way Fusion

Prototype bank and assignment. Our representation is organized around a small bank of $K_{\max}=12$ learnable prototypes $\{\mathbf{p}_k\}_{k=1}^{K_{\max}}$, each acting as a soft detector for a recurring aerial region (buildings, vegetation, roads, water); the per-image saliency gate (next paragraph) selects an active subset of typical size $K=10$, so K_{\max} is the bank capacity and K the typical active count throughout the paper. Each projected, altitude-modulated patch token \mathbf{z}_i commits to one prototype through a single-pass temperature-scaled cosine assignment

$$\mathbf{A}_{i,k} = \frac{\exp(\langle \bar{\mathbf{p}}_k, \bar{\mathbf{z}}_i \rangle / \tau)}{\sum_j \exp(\langle \bar{\mathbf{p}}_j, \bar{\mathbf{z}}_i \rangle / \tau)}, \quad (1)$$

¹The CLS (classification) token is a learnable, special vector added to the input sequence of a Vision Transformer (ViT) to represent the entire image for classification tasks [Lappe and Giese, 2025].

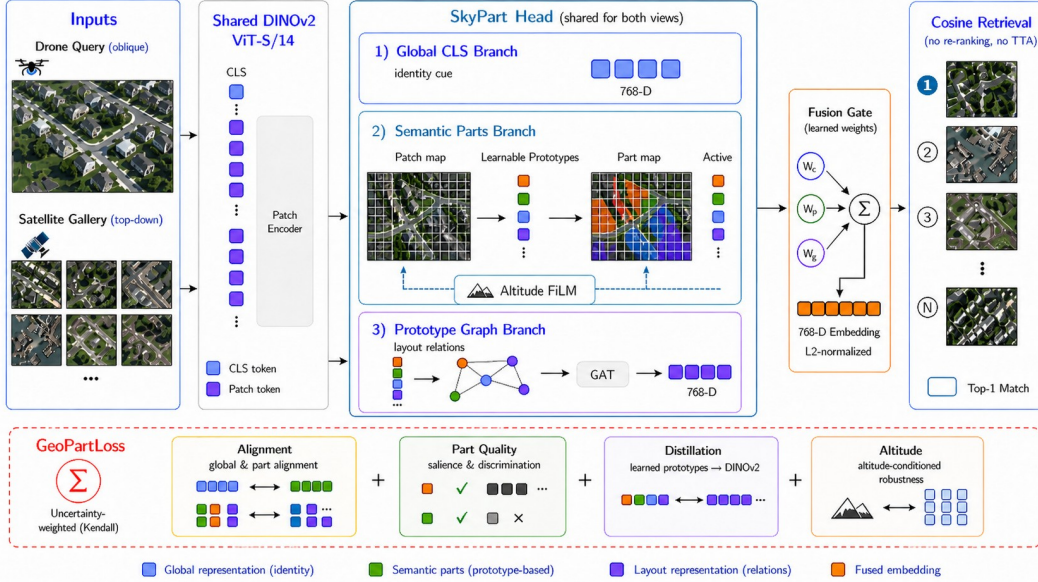


Figure 1: **SKYPART overview.** A shared DINOv2 ViT-S/14 encodes drone and satellite views; three readouts (global CLS, semantic parts with K learnable prototypes under altitude-conditioned FiLM, and a prototype GAT for layout) are merged by a learned fusion gate into a 768-D ℓ_2 -normalised embedding, retrieved by cosine similarity in one pass (no re-ranking, no TTA). *Bottom:* training-only GEOPARTLOSS with four uncertainty-weighted (Kendall) groups (Alignment, Part Quality, Distillation, Altitude); inference uses mean FiLM and no altitude metadata.

where $\bar{\mathbf{p}}_k$ and $\bar{\mathbf{z}}_i$ denote the ℓ_2 -normalized prototype and patch token (so $\langle \bar{\mathbf{p}}_k, \bar{\mathbf{z}}_i \rangle$ is a cosine similarity); the softmax runs *over prototype indices* rather than over patch positions, which is what turns the bank into a competing set of slots [Locatello et al., 2020] rather than a linear reweighting. Prototype count, dimensionality, and temperature are given in Appendix A2.1.

Per-image salience gating. Because different scenes activate different subsets of the bank (an urban tile rarely needs a “water” prototype), we learn a per-image Gumbel-sigmoid salience gate over the prototype indices that zeroes out inactive prototypes at the image level while keeping a small active set. The gate, the residual MLP that refines each active part, and the spatial-centroid bookkeeping are detailed in Appendix A1.3.

Three-way fusion. The retrieval embedding combines three readouts. A global branch keeps the CLS token (\mathbf{f}_{cls}), a part branch pools the salience-weighted part descriptors into \mathbf{f}_{part} , and a graph branch passes the active prototype nodes through a two-layer GAT [Veličković et al., 2018] over a fully-connected adjacency (feasible for this small prototype bank) to yield a layout readout $\mathbf{f}_{\text{graph}}$. The part and CLS pathways carry identity-heavy information (what the components are), and the graph readout carries arrangement-heavy information (how they are related), consistent with the layout-invariance framing of Sec. 1 and formalized as an information-bottleneck factorization in Appendix A1.2. A lightweight gating MLP learns non-negative weights summing to one, with

$$[w_p, w_c, w_g] = \text{softmax}(\mathbf{W}_2 \text{ReLU}(\mathbf{W}_1 [\mathbf{f}_{\text{part}}; \mathbf{f}_{\text{cls}}; \mathbf{f}_{\text{graph}}])), \quad (2)$$

initialized to start biased toward the part branch and re-balance during training. The output is the L2-normalized sum $\mathbf{f} = \text{L2Norm}(w_p \mathbf{f}_{\text{part}} + w_c \mathbf{f}_{\text{cls}} + w_g \mathbf{f}_{\text{graph}})$.

3.3 Altitude as a Training-Time Nuisance (FiLM)

Altitude changes scale and perspective but is not part of the location identity we want the retrieval embedding to encode, so we treat it as a nuisance to marginalize rather than a feature to keep. During training, FiLM conditions projected patch tokens on the available altitude bin before prototype assignment. At inference, no altitude input is used: altitude-specific FiLM parameters are replaced by their marginalized mean and this fixed modulation is applied to both views. Thus the deployed embedding has no dependence on test-time altitude metadata, while still benefiting from altitude-aware regularization during training. The formal mean-FiLM argument is given in Appendix A1.2.

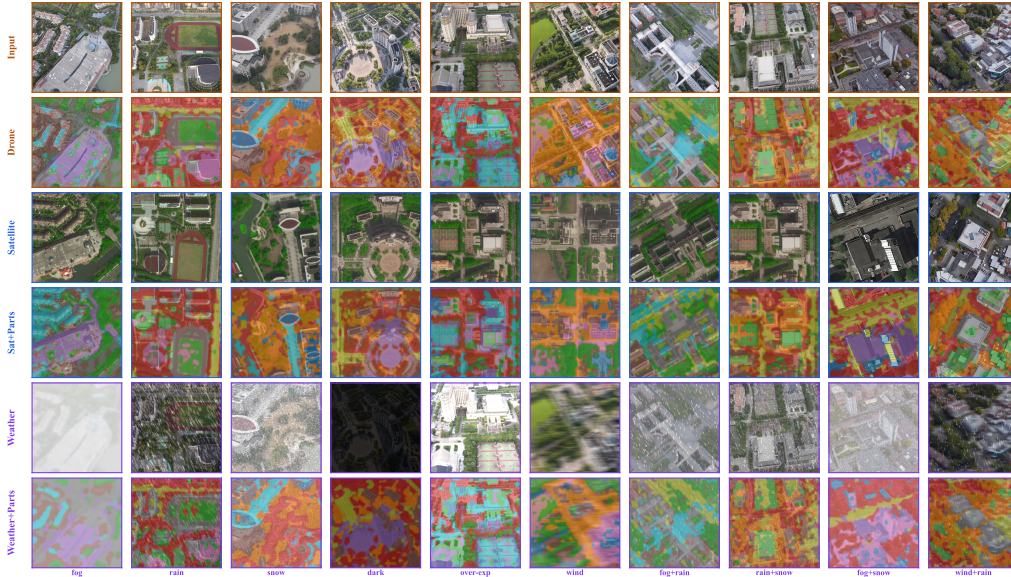


Figure 2: **Part-level evidence under weather shifts.** Rows show clean drone inputs, their part-level activations, paired satellite views, satellite part activations, weather-corrupted drone queries, and the corresponding part activations. Columns cover different corruptions and mixed weather conditions. Across substantial appearance changes, the part-discovery head continues to produce spatially structured activations over buildings, roads, fields, and open regions, rather than collapsing to a single dominant texture cue. These visualizations support prototype-based layout as a robust cross-view abstraction learned from the retrieval objective alone, without segmentation supervision.

Masked Part Reconstruction and distillation further shape the part pathway during training and are detailed in Appendix A1.3.

3.4 Novel Training Objective: GEOPARTLOSS

GeoPartLoss. We use a novel multi-objective training loss that jointly optimizes four complementary objectives via Kendall homoscedastic uncertainty weighting [Kendall et al., 2018]: $\mathcal{L}_{\text{GEOPARTLOSS}} = \sum_{g \in \mathcal{G}} [\exp(-s_g) \mathcal{L}_g + s_g]$, where $\mathcal{G} = \{\text{align, part, distill, alt}\}$ are the four loss groups, and $s_g = \log \sigma_g^2$ is a per-group learnable log-variance. The weight $\exp(-s_g)$ is always positive, so a larger s_g down-weights that group; the additive s_g term penalizes collapse to zero. By construction, any stationary point of this loss is a Pareto-stationary point of the four-objective vector $(\mathcal{L}_{\text{align}}, \mathcal{L}_{\text{part}}, \mathcal{L}_{\text{distill}}, \mathcal{L}_{\text{alt}})$ [Sener and Koltun, 2018], removing the need for hand-tuned loss scalars.

Four loss groups. (i) *Alignment* ($\mathcal{L}_{\text{align}}$): Circle loss [Sun et al., 2020], proxy-anchor [Kim et al., 2020], and InfoNCE [van den Oord et al., 2018] applied to the fused 768-D embedding, pulling same-location drone–satellite pairs together and pushing different-location pairs apart. (ii) *Part quality* ($\mathcal{L}_{\text{part}}$): masked part reconstruction (MAR) and prototype diversity, encouraging prototypes to cover distinct and semantically meaningful scene regions. (iii) *Distillation* ($\mathcal{L}_{\text{distill}}$): feature-level alignment toward a frozen DINOv2 ViT-B/14 teacher and an exponential moving average (EMA) self-ensemble [Tarvainen and Valpola, 2017], providing a stable training signal for the smaller student backbone. (iv) *Altitude* (\mathcal{L}_{alt}): SmoothL1 regression on normalized altitude, active only when metadata is available and omitted otherwise. More details of this loss can be found in Appendix A1.5.

Uncertainty-Aware Proxy Alignment (UAPA). Within the alignment group, we modulate the distillation temperature using the relative entropy gap between the drone and satellite proxy distributions. More uncertain drone queries receive softer teacher targets while confident queries retain the default temperature, with gradient magnitude preserved. Full formulation and ablation are in Appendix A1.4.

Inference. SKYPART reduces at test time to a single forward pass through the backbone and head. The teacher, EMA self-ensemble, altitude-supervision branch, and all GEOPARTLOSS terms are discarded; altitude-specific FiLM is replaced by fixed mean-FiLM parameters requiring no altitude

Table 1: **SUES-200 per-altitude comparison.** R@1/AP (%) at four UAV altitudes for D→S and S→D, with mean R@1 per direction in the rightmost column of each block. SKYPART is evaluated with a single-scale 448×448 crop, the full 200-satellite confusion gallery, and no post-processing; non-SKYPART numbers are reported from the original publications. Cell shading scales with R@1/AP (green = high, red = low). **Red:** best; **blue:** second; SKYPART has the lowest Params/GFLOPs.

Method	Venue	Params↓	GFLOPs↓	Drone→Satellite								Satellite→Drone									
				150m		200m		250m		300m		150m		200m		250m		300m		Mean	
				R@1	AP	R@1	AP	R@1	AP	R@1	AP	R@1	AP	R@1	AP	R@1	AP	R@1	AP		
LPN [Wang et al., 2022]	TCSVT'22	62.4 M	36.78	61.58	67.23	70.85	75.96	80.38	83.80	81.47	84.53	73.57	83.75	66.78	88.75	75.01	92.50	81.34	92.50	85.72	89.38
Baseline [Zhu et al., 2023]	TCSVT'23	-	-	55.65	61.92	66.78	71.55	72.00	76.43	74.05	78.26	67.12	75.00	55.46	85.00	66.05	86.25	69.94	88.75	74.46	83.75
Sample4Geo [Deuser et al., 2023]	ICCV'23	87.6 M	90.24	92.60	94.00	97.38	97.81	98.28	98.64	99.18	99.36	96.86	92.50	94.00	97.38	97.81	98.28	98.64	99.18	99.36	96.84
MCCG [Shen et al., 2024]	TCSVT'24	56.6 M	51.04	82.22	85.47	89.38	91.41	93.82	95.04	95.07	96.20	90.12	93.75	89.72	93.75	92.21	96.25	96.14	98.75	96.64	95.62
SeGCN [Liu et al., 2024]	JSTARS'24	28.0 M	24.58	90.80	92.32	91.93	93.41	92.53	93.90	93.33	94.61	92.15	93.75	92.45	95.00	93.65	96.25	94.39	97.50	94.55	95.62
CCR [Du et al., 2024]	TCSVT'24	156.6 M	160.6	87.08	89.55	93.57	94.90	95.42	96.28	96.82	97.39	93.22	92.50	88.54	97.50	95.22	97.50	97.10	97.50	97.49	96.25
CAMP [Wu et al., 2024]	TGRS'24	91.4 M	90.24	95.40	96.38	97.63	98.16	98.05	98.45	99.33	99.46	97.60	96.25	93.69	97.50	96.76	98.75	98.10	100.00	98.85	98.12
DAC [Xia et al., 2024]	TCSVT'24	96.5 M	90.24	96.80	97.54	97.48	97.97	98.20	98.62	97.58	98.14	97.52	97.50	94.06	98.75	96.66	98.75	98.09	98.75	97.87	98.44
MEAN [Chen et al., 2025]	TGRS'25	36.5 M	26.18	95.50	96.46	98.38	98.72	98.95	99.17	99.52	99.63	98.09	97.50	94.75	100.00	97.09	100.00	98.28	100.00	99.21	99.38
SKYPART (Ours)	-	26.95 M	22.14	97.25	97.90	98.75	99.33	99.30	99.64	99.60	99.77	98.74	100.00	97.36	100.00	97.95	100.00	99.98	100.00	99.95	100.00

metadata. The deployed model is the 26.95 M student and its 768-D embedding. Retrieval uses cosine similarity with no re-ranking, TTA, query expansion, multi-crop inference, or post-processing.

4 Experiments

4.1 Datasets and Protocol

We evaluate SKYPART on SUES-200 [Zhu et al., 2023], University-1652 [Zheng et al., 2020], and DenseUAV [Dai et al., 2024] under a strict single-pass protocol: a single-scale 448×448 crop, the full confusion gallery when defined by the benchmark, and no test-time augmentation, re-ranking, query expansion, multi-crop inference, or other post-processing. Published baselines in the SOTA tables are reported from their original papers and may follow method-specific protocols, as detailed in Sec. 4.3. Altitude is treated as an optional training-time nuisance signal, not a required input feature. We use FiLM bins when metadata is available (150/200/250/300 m on SUES-200; dataset-provided altitude bins on DenseUAV), and mean-FiLM otherwise, omitting the altitude-supervision term on datasets without altitude labels. Thus the same head supports datasets with and without altitude annotations without pseudo-labeling or folder-derived heuristics. For weather robustness we adopt the WeatherPrompt protocol [Wen et al., 2025] verbatim. Split sizes, per-method weather fine-tuning recipes, and dataset quirks appear in Appendix A2.2 and A3.4. All results use official splits and full benchmark galleries. WeatherPrompt corrupts drone queries only.

4.2 Implementation Details

The deployed model is a DINOv2 ViT-S/14 student with the SKYPART head, totaling 26.95 M parameters and 22.14 GFLOPs for a single 448×448 forward pass. Training uses AdamW, identity-balanced mini-batches, standard crop/colour augmentation, and the GEOPARTLOSS groups described in Sec. 3.4. DenseUAV additionally uses rotation augmentation during training because its satellite crops have arbitrary basemap orientation; SUES-200 and University-1652 use canonical orientations. At inference, the teacher, EMA, FiLM-altitude auxiliaries, and all training objectives are discarded; retrieval is cosine similarity between 768-D embeddings, with no re-ranking, TTA, query expansion, multi-crop inference, or post-processing. Results for SKYPART follow this deployed protocol. Full hyperparameters and dataset-specific training details are in Appendix A2.1 and Appendix A2.2.

4.3 Comparison with State of the Art

SUES-200. Table 1 reports the SUES-200 comparison. Even under a deliberately handicapped protocol-single 448×448 crop, one forward pass, the full 200-tile confusion gallery, and *no* re-ranking, TTA, query expansion, or multi-crop inference, while baselines retain whatever inference-time wrappers their original papers use-SKYPART sets a new state of the art across every altitude band on D→S with the smallest model in the table. The margin grows at the lowest altitude, where the field of view is narrow and only partial facades are visible: global descriptors lose traction precisely in the regime where part-level layout becomes the deciding cue, exactly as the framing in Sec. 1 predicts.

University-1652 and DenseUAV. Table 2 extends the same picture to the other two benchmarks. On University-1652, SKYPART leads R@1 and AP at the lowest parameter budget in the comparison while running the inference path with mean-FiLM (no altitude metadata), evidence that the architecture itself, rather than altitude conditioning, carries the advantage. DenseUAV is the harder benchmark-its

Table 2: **University-1652 (left) and DenseUAV (right)**. Side-by-side state-of-the-art comparison. SKYPART leads both benchmarks while remaining among the smallest models in the comparison. Same cell shading as Table 1 (green = high R@1/AP). **Red**: best; **blue**: second. [†]DenseUAV: 256×256 input; *param count estimated from backbone (ViT-S≈22 M, ConvNeXt-T≈28 M, ConvNeXt-B≈88 M, DINOv2-B≈86 M).

(a) University-1652							(b) DenseUAV					
Method	Venue	Params	D→S		S→D		Method	Venue	Params	R@1	R@5	SDM@1
			R@1	AP	R@1	AP						
LPN [Wang et al., 2022]	TCSVT'22	62.4 M	77.71	80.80	90.30	78.78	DenseUAV baseline [†] [Dai et al., 2024]	TIP'23	~22 M*	83.01	95.58	86.50
Sample4Geo [Deuser et al., 2023]	ICCV'23	87.6 M	92.65	93.81	95.14	91.39	Sample4Geo [†] [Deuser et al., 2023]	ICCV'23	87.6 M	49.38	78.29	61.72
MCCG [Shen et al., 2024]	TCSVT'24	56.6 M	89.40	91.07	94.29	89.29	MCCG [†] [Shen et al., 2024]	TCSVT'24	~28 M*	83.14	93.39	85.94
CCR [Du et al., 2024]	TCSVT'24	156.6 M	92.54	93.78	95.15	91.80	CAMP [†] [Wu et al., 2024]	TGRS'24	91.4 M	88.72	–	–
CAMP [Wu et al., 2024]	TGRS'24	91.0 M	94.46	95.38	96.15	92.72	Yang et al. [†] [Yang et al., 2025]	RA-L'25	~86 M*	86.27	96.33	88.87
MEAN [Chen et al., 2025]	TGRS'25	36.5 M	93.55	94.53	96.01	92.08	CEUSP [†] [Xu et al., 2025b]	PRCV'25	~28 M*	89.45	96.05	91.01
MEAN [Chen et al., 2025]	TGRS'25	36.5 M	90.18	–	–	–	MEAN [†] [Chen et al., 2025]	TGRS'25	36.5 M	90.18	–	–
SKYPART (Ours)	–	26.95 M	96.47	97.77	98.43	98.24	SKYPART (Ours)	–	26.95 M	91.85	97.81	93.59

dense urban gallery makes neighbouring locations visually ambiguous and three flight heights stress the altitude module-yet SKYPART still ranks first on both R@1 and SDM@1, with the previous best methods trailing on both metrics simultaneously rather than splitting them.

Protocol note for Tables 1 and 2. SKYPART is evaluated under the strict single-pass protocol of Sec. 4.2; the baseline numbers are taken directly from each original publication, where many entries lean on inference-time wrappers such as k-reciprocal re-ranking, multi-scale TTA, query expansion, larger inputs, or larger backbones, all of which routinely add several R@1 points on top of a frozen embedding. We deliberately do not apply any such wrappers to SKYPART, so the comparison is structurally unfavourable to us: we outperform baselines that already enjoy those advantages, and the gap to a fully protocol-normalized re-run would only widen.

4.4 Weather Robustness (WeatherPrompt)

Clean-data accuracy is a weak proxy for a drone flying through fog at dusk. WeatherPrompt [Wen et al., 2025] stress-tests this setting by applying ten weather and visibility corruptions to the drone query while keeping the satellite gallery clean. Since the deployment-critical direction is drone-query localization, Table 3 reports D→S R@1 on SUES-200, University-1652, and DenseUAV; full per-condition R@1/AP results for both D→S and S→D are deferred to Appendix A3.4.

On SUES-200 and University-1652, baselines are reported from WeatherPrompt at 384×384, while SKYPART is retrained at 392×392 (yielding a 28×28 patch grid for DINOv2 ViT-S/14) under the same corruption pipeline, so these two blocks should be read as reported-baseline rather than fully resolution-controlled comparisons. On DenseUAV, we apply the same WeatherPrompt pipeline to reproduced baselines and SKYPART; SKYPART also ranks first on this denser urban robustness benchmark. Across all datasets, SKYPART preserves the highest mean robustness and degrades most under combined visibility failures such as fog+snow and darkness, showing evidence that layout survives texture corruption better than global descriptors.

4.5 Ablation Study

Table 4 sweeps four ablation axes (loss-group removal, representation branch, prototype salience, paired UAPA) under the same D→S weather-online evaluation as Table 3. Blocks A–C share an ablation-baseline checkpoint (Mean R@1 96.03%) trained with the matched weather-online recipe, which is a separate training run from the deployed weather-benchmark checkpoint of Table 3 (Mean 94.71%). The two share architecture and recipe family but not seeds, so within-table deltas, rather than absolute scores, are the comparable quantity; Block D is paired separately and read by its within-block delta.

Block A (GEOPARTLOSS groups). Cross-view alignment is the dominant training signal: removing the alignment group is catastrophic (Mean R@1 collapses by tens of points), while removing part quality, altitude, or distillation each costs only about a point of Mean R@1. The asymmetry shows that GEOPARTLOSS factorizes cleanly: alignment is the signal-carrying head, and the three auxiliary heads regularize and calibrate it, paying off under stress conditions rather than on Normal weather.

Block B (representation branch). The *CLS readout only* variant still trains the full head end-to-end (gradients still shape the backbone) and only drops the part and graph readouts at retrieval; even with

Table 3: **Weather robustness summary.** Drone→Satellite R@1 (%) under the 10-condition WeatherPrompt corruption pipeline with clean satellite galleries. SUES-200 and University-1652 baselines are reported from WeatherPrompt [Wen et al., 2025] at 384×384; SKYPART is retrained at 392×392. DenseUAV uses the same corruption pipeline with reproduced baselines, yielding a third weather-robustness benchmark. Full results for D→S and S→D are in Appendix A3.4. **Red**: best; **blue**: second.

Method	Venue	Params↓	Normal	Fog	Rain	Snow	F+R	F+S	R+S	Dark	Over-exp	Wind	Mean
SUES-200													
Sample4Geo [†] [Deuser et al., 2023]	ICCV'23	87.6 M	74.93	72.58	34.60	28.95	35.10	12.95	20.05	34.18	38.40	67.80	41.95
Safe-Net* [Lin et al., 2025]	TIP'25	25.6 M	76.31	73.53	54.15	48.94	45.12	40.05	25.95	29.74	54.86	58.10	50.68
CCR [†] [Du et al., 2024]	TCSVT'24	156.6 M	73.22	70.95	60.14	50.31	45.87	45.80	31.25	31.03	59.97	52.02	52.06
WeatherPrompt [Wen et al., 2025]	NeurIPS'25	87.6 M	76.72	68.49	71.77	59.95	58.24	64.36	58.49	40.42	61.57	65.19	62.52
SKYPART (Ours)	–	26.95 M	97.21	96.27	96.06	95.33	94.71	90.44	95.17	92.06	93.34	96.54	94.71
University-1652													
Sample4Geo* [Deuser et al., 2023]	ICCV'23	87.6 M	92.70	88.70	62.44	52.76	52.70	19.79	38.19	46.34	75.77	81.54	61.10
Safe-Net* [Lin et al., 2025]	TIP'25	25.6 M	86.98	82.12	67.13	60.50	54.80	32.12	25.83	41.10	69.87	74.32	59.48
CCR [†] [Du et al., 2024]	TCSVT'24	156.6 M	92.54	85.57	67.46	55.16	63.11	27.74	23.06	51.10	75.90	81.31	62.30
WeatherPrompt [Wen et al., 2025]	NeurIPS'25	87.6 M	82.78	81.46	80.34	77.60	78.75	73.38	78.41	67.22	74.20	77.26	77.14
SKYPART (Ours)	–	26.95 M	95.15	93.78	93.44	92.05	90.05	88.51	89.47	83.26	88.23	89.68	90.36
DenseUAV													
Sample4Geo [†] [Deuser et al., 2023]	ICCV'23	87.6 M	72.37	72.42	73.66	72.80	73.14	70.44	72.59	66.50	69.76	72.29	71.60
Safe-Net* [Lin et al., 2025]	TIP'25	25.6 M	41.14	39.47	40.11	37.11	37.54	31.87	39.30	33.20	37.07	40.03	37.68
CCR [†] [Du et al., 2024]	TCSVT'24	156.6 M	56.76	55.21	55.94	54.70	54.10	51.48	55.30	49.85	54.44	54.87	54.26
WeatherPrompt [Wen et al., 2025]	NeurIPS'25	87.6 M	26.25	24.15	26.68	24.28	25.35	20.72	25.10	20.08	22.48	25.78	24.09
SKYPART (Ours)	–	26.95 M	91.25	90.13	91.38	90.35	89.79	87.69	91.12	84.64	90.18	91.76	89.83

Table 4: **Weather-aligned ablation on SUES-200 (Drone→Satellite).** [†]Full (Ours) is the single reference row; all Δ Mean values in blocks A–C are computed against it. Block D is a paired run and its Δ is within-block only. Blocks A–C share one ablation checkpoint (Normal 98.69, Mean 96.03), trained separately from the deployed checkpoint of Table 3 (Normal 97.21, Mean 94.71) — the 1.5 pp normal gap reflects the modest clean-accuracy cost of weather-online training. **Red** \blacktriangleleft : catastrophic drop (>10 pp); **blue** \blacktriangleleft : large drop (2–10 pp); gray: minor (<2 pp). Training follows the matched weather-online recipe. Deltas in the text are computed against the corresponding full-model row. Weather-run implementation details are in Appendix A3.4.

Configuration	Normal		Fog		Rain		Snow		F+R		F+S		R+S		Dark		Over-exp		Wind		Mean	Δ Mean	
	R@1	AP	R@1	AP	R@1	AP	R@1	AP	R@1	AP	R@1	AP	R@1	AP	R@1	AP	R@1	AP	R@1	AP			
Full (Ours)[†]	98.69	99.23	97.84	98.75	97.19	98.43	96.41	97.94	95.90	97.69	92.31	95.27	95.53	97.43	93.09	95.37	95.91	97.60	97.46	98.54	96.03	97.62	—
A. GeoPartLoss group removal																							
– C_{align}	54.49	66.02	34.49	47.21	21.56	33.75	16.76	29.27	17.58	28.20	7.24	16.36	13.24	23.98	29.52	41.73	45.01	57.62	36.83	50.04	27.67	39.42	–68.4 \blacktriangleleft
– C_{part}	97.28	98.28	96.39	97.78	96.51	97.92	95.58	97.25	95.14	97.00	90.89	94.12	95.36	97.11	91.30	94.04	94.31	96.45	96.48	97.85	94.92	96.78	–1.1
– C_{alt}	97.47	98.45	96.96	98.17	96.84	98.15	95.59	97.38	95.46	97.25	90.98	94.12	95.63	97.35	92.41	94.88	94.19	96.49	96.68	98.07	95.22	97.03	–0.8
– $C_{distill}$	97.63	98.56	96.70	98.03	96.16	97.72	95.36	97.17	94.16	96.44	89.42	92.95	94.77	96.77	91.79	94.40	94.32	96.53	96.24	97.77	94.65	96.64	–1.4
B. Representation branch																							
CLS readout only	93.56	96.10	90.43	94.15	87.55	92.29	87.39	92.09	84.01	89.56	73.19	81.26	84.78	90.15	81.91	87.56	86.20	91.09	87.34	91.95	85.64	90.62	–10.4 \blacktriangleleft
Part branch only	97.51	98.58	96.19	97.81	95.54	97.35	94.69	96.87	93.13	95.90	88.10	92.34	93.58	96.06	91.98	94.58	94.40	96.66	95.73	97.41	94.09	96.36	–1.9
w/o Graph branch	97.56	98.28	96.88	97.90	96.06	97.46	95.33	97.06	94.35	96.46	90.51	93.87	95.24	96.99	91.61	94.12	94.98	96.67	96.10	97.48	94.86	96.63	–1.2
C. Prototype salience gate																							
All prototypes active	97.79	98.62	96.81	98.09	95.44	97.24	95.34	97.08	93.08	95.81	86.44	91.24	93.32	95.81	90.55	93.57	92.86	95.60	95.54	97.25	93.72	96.03	–2.3 \blacktriangleleft
D. UAPA (paired run; Δ within-block only)																							
w/o UAPA	96.92	98.10	95.64	97.39	94.91	97.04	94.74	96.93	93.22	95.97	89.23	93.23	93.43	96.07	91.71	94.43	93.37	95.96	95.68	97.37	93.88	96.25	–1.1
w/ UAPA (paired)	98.06	98.88	96.85	98.15	96.16	97.68	95.84	97.50	94.34	96.62	89.60	93.37	94.73	96.74	92.93	95.22	94.42	96.73	96.48	97.95	94.94	96.88	—

this advantage, mean R@1 falls by roughly ten points relative to Full, with the largest gap on the hardest combined corruptions where layout is the only signal that survives texture loss. Reintroducing the part branch recovers most of the gap and the graph branch supplies the rest, supporting the identity/arrangement factorization motivated in Sec. 1. These Block B numbers differ from the CLS-only backbone-ablation baselines in Appendix A3.3, which strip the head from training entirely (no part/graph gradients during training) and therefore sit several points lower.

Block C (prototype salience). Disabling the salience gate while keeping the same prototype bank and graph readout (*All prototypes active*) costs about two points of Mean R@1, isolating the gain that comes from learning *which* prototypes matter per image rather than merely from prototype capacity. *Block D (paired UAPA).* On the paired seed/checkpoint run, uncertainty-aware temperature modulation lifts within-block Mean R@1 by roughly a point and Mean AP by half a point; we read this delta as the contribution of UAPA in isolation, without conflating it with the canonical benchmark score. Backbone-substrate controls (DINOv2 / iBOT / MoCo v3 ViT-S) are deferred to Appendix A3.3.

5 Conclusion

We built SKYPART around the principle that aerial cross-view matching should factor texture out and preserve layout, and instantiated it as a lightweight part-discovery head for patch-based ViTs. Under a strict single-pass protocol (no re-ranking, no TTA), SKYPART sets the new state of the art on SUES-200, University-1652, and DenseUAV while remaining among the most parameter-efficient methods in the comparison, and its margin grows under the ten WeatherPrompt corruption conditions [Wen et al., 2025]. The ablations (Sec. 4.5) confirm the predicted hierarchy: alignment carries the retrieval signal, the three-way fusion absorbs most of the weather-induced drop, and altitude-FiLM acts as a training-time regularizer with no inference dependency. Zero-shot University-1652→SUES-200 transfer (Appendix A3.5) leads on D→S and remains competitive on S→D, supporting explicit grouping as a complement to global pooling. Broader impacts are in Appendix A4.2.

Acknowledgments and Disclosure of Funding

All experiments were run on a single NVIDIA A100 80 GB GPU.

References

- Alessandro Achille and Stefano Soatto. Emergence of invariance and disentanglement in deep representations. *Journal of Machine Learning Research*, 19(50):1–34, 2018. URL <https://www.jmlr.org/papers/v19/17-646.html>.
- Relja Arandjelović, Petr Gronat, Akihiko Torii, Tomas Pajdla, and Josef Sivic. NetVLAD: CNN architecture for weakly supervised place recognition. In *Proceedings of the IEEE Conference on Computer Vision and Pattern Recognition (CVPR)*, 2016. URL https://openaccess.thecvf.com/content_cvpr_2016/html/Arandjelovic_NetVLAD_CNN_Architecture_CVPR_2016_paper.html.
- Alexei Baevski, Wei-Ning Hsu, Qiantong Xu, Arun Babu, Jiatao Gu, and Michael Auli. data2vec: A general framework for self-supervised learning in speech, vision and language. In *Proceedings of the International Conference on Learning Representations (ICLR)*, 2022. doi: 10.48550/arXiv.2202.03555.
- Irving Biederman. Recognition-by-components: A theory of human image understanding. *Psychological Review*, 94(2):115–147, 1987. doi: 10.1037/0033-295X.94.2.115.
- Mathilde Caron, Hugo Touvron, Ishan Misra, Hervé Jégou, Julien Mairal, Piotr Bojanowski, and Armand Joulin. Emerging properties in self-supervised vision transformers. In *Proceedings of the IEEE/CVF International Conference on Computer Vision (ICCV)*, pages 9650–9660, 2021. doi: 10.1109/ICCV48922.2021.00951. URL https://openaccess.thecvf.com/content/ICCV2021/html/Caron_Emerging_Properties_in_Self-Supervised_Vision_Transformers_ICCV_2021_paper.html.
- Quan Chen, Tingyu Wang, Zihao Yang, Haoran Li, Rongfeng Lu, Yaoqi Sun, Bolun Zheng, and Chenggang Yan. SDPL: Shifting-dense partition learning for UAV-view geo-localization. *IEEE Transactions on Circuits and Systems for Video Technology*, 34(11):11810–11824, 2024. doi: 10.1109/TCSVT.2024.3424196.
- Ting Chen, Simon Kornblith, Mohammad Norouzi, and Geoffrey Hinton. A simple framework for contrastive learning of visual representations. In *International Conference on Machine Learning (ICML)*, 2020. URL <https://proceedings.mlr.press/v119/chen20j.html>.
- Xinlei Chen, Saining Xie, and Kaiming He. An empirical study of training self-supervised vision transformers. In *Proceedings of the IEEE/CVF International Conference on Computer Vision (ICCV)*, 2021. URL https://openaccess.thecvf.com/content/ICCV2021/papers/Chen_An_Empirical_Study_of_Training_Self-Supervised_Vision_Transformers_ICCV_2021_paper.pdf.
- Zhongwei Chen, Zhao-Xu Yang, and Hai-Jun Rong. Multilevel embedding and alignment network with consistency and invariance learning for cross-view geo-localization. *IEEE Transactions on Geoscience and Remote Sensing*, 63:1–15, 2025. doi: 10.1109/TGRS.2025.3572775.

- Taco Cohen and Max Welling. Group equivariant convolutional networks. In *International Conference on Machine Learning (ICML)*, 2016. URL <https://proceedings.mlr.press/v48/cohenc16.html>.
- Andy Couturier and Moulay A. Akhlofi. A review on absolute visual localization for UAV. *Robotics and Autonomous Systems*, 135:103666, 2021. doi: 10.1016/j.robot.2020.103666.
- Ming Dai, Jianhong Hu, Jiedong Zhuang, and Enhui Zheng. A transformer-based feature segmentation and region alignment method for UAV-view geo-localization. *IEEE Transactions on Circuits and Systems for Video Technology*, 32(7):4376–4389, 2022. doi: 10.1109/TCSVT.2021.3135013.
- Ming Dai, Enhui Zheng, Zhenhua Feng, Lei Qi, Jiedong Zhuang, and Wankou Yang. Vision-based UAV self-positioning in low-altitude urban environments. *IEEE Transactions on Image Processing*, 33:493–508, 2024. doi: 10.1109/TIP.2023.3346279.
- Fabian Deuser, Konrad Habel, and Norbert Oswald. Sample4Geo: Hard negative sampling for cross-view geo-localisation. In *Proceedings of the IEEE/CVF International Conference on Computer Vision (ICCV)*, pages 16801–16810, 2023. doi: 10.1109/ICCV51070.2023.01545.
- Alexey Dosovitskiy, Lucas Beyer, Alexander Kolesnikov, Dirk Weissenborn, Xiaohua Zhai, Thomas Unterthiner, Mostafa Dehghani, Matthias Minderer, Georg Heigold, Sylvain Gelly, Jakob Uszkoreit, and Neil Houlsby. An image is worth 16x16 words: Transformers for image recognition at scale. In *Proceedings of the International Conference on Learning Representations (ICLR)*, 2021. doi: 10.48550/arXiv.2010.11929.
- Haolin Du, Jingfei He, and Yuanqing Zhao. CCR: A counterfactual causal reasoning-based method for cross-view geo-localization. *IEEE Transactions on Circuits and Systems for Video Technology*, 34(11):11630–11643, 2024. doi: 10.1109/TCSVT.2024.3425509.
- Vincent Dumoulin, Ethan Perez, Nathan Schucher, Florian Strub, Harm de Vries, Aaron Courville, and Yoshua Bengio. Feature-wise transformations. *Distill*, 2018. doi: 10.23915/distill.00011.
- Tongtong Feng, Qing Li, Xin Wang, Mingzi Wang, Guangyao Li, and Wenwu Zhu. Multi-weather cross-view geo-localization using denoising diffusion models. In *Proceedings of the 2nd Workshop on UAVs in Multimedia (UAVM)*, pages 35–39, 2024. doi: 10.1145/3689095.3689103.
- Yaroslav Ganin and Victor Lempitsky. Unsupervised domain adaptation by backpropagation. In *International Conference on Machine Learning (ICML)*, 2015. doi: 10.48550/arXiv.1409.7495.
- Yuan Gao, Haibo Liu, and Xiaohui Wei. Semantic concept perception network with interactive prompting for cross-view image geo-localization. *IEEE Transactions on Circuits and Systems for Video Technology*, 35(6):5343–5354, 2025. doi: 10.1109/TCSVT.2025.3533574.
- Fawei Ge, Yunzhou Zhang, Li Wang, Wei Liu, Yixiu Liu, Sonya Coleman, and Dermot Kerr. Multilevel feedback joint representation learning network based on adaptive area elimination for cross-view geo-localization. *IEEE Transactions on Geoscience and Remote Sensing*, 62:1–15, 2024. doi: 10.1109/TGRS.2024.3396330.
- Jianping Gou, Baosheng Yu, Stephen J. Maybank, and Dacheng Tao. Knowledge distillation: A survey. *International Journal of Computer Vision*, 129:1789–1819, 2021. doi: 10.1007/s11263-021-01453-z.
- Kaiming He, Xinlei Chen, Saining Xie, Yanghao Li, Piotr Dollár, and Ross Girshick. Masked autoencoders are scalable vision learners. In *Proceedings of the IEEE/CVF Conference on Computer Vision and Pattern Recognition (CVPR)*, pages 16000–16009, 2022. URL https://openaccess.thecvf.com/content/CVPR2022/html/He_Masked_Autoencoders_Are_Scalable_Vision_Learners_CVPR_2022_paper.
- Geoffrey Hinton, Oriol Vinyals, and Jeff Dean. Distilling the knowledge in a neural network. *arXiv preprint arXiv:1503.02531*, 2015. doi: 10.48550/arXiv.1503.02531. NIPS 2015 Deep Learning Workshop.
- Kaiji Hou, Qiang Tong, Na Yan, Xiulei Liu, and Shoulu Hou. MCFA: Multi-scale cascade and feature adaptive alignment network for cross-view geo-localization. *Sensors*, 25(14):4519, 2025. doi: 10.3390/s25144519.

- Sixing Hu, Mengdan Feng, Rang M. H. Nguyen, and Gim Hee Lee. CVM-net: Cross-view matching network for image-based ground-to-aerial geo-localization. In *Proceedings of the IEEE Conference on Computer Vision and Pattern Recognition (CVPR)*, 2018. URL https://openaccess.thecvf.com/content_cvpr_2018/html/Hu_CVM-Net_Cross-View_Matching_CVPR_2018_paper.html.
- Alex Kendall, Yarin Gal, and Roberto Cipolla. Multi-task learning using uncertainty to weigh losses for scene geometry and semantics. In *Proceedings of the IEEE/CVF Conference on Computer Vision and Pattern Recognition (CVPR)*, pages 7482–7491, 2018. URL https://openaccess.thecvf.com/content_cvpr_2018/html/Kendall_Multi-Task_Learning_Using_CVPR_2018_paper.html.
- Sungyeon Kim, Dongwon Kim, Minsu Cho, and Suha Kwak. Proxy anchor loss for deep metric learning. In *Proceedings of the IEEE/CVF Conference on Computer Vision and Pattern Recognition (CVPR)*, pages 3238–3247, 2020. doi: 10.48550/arXiv.2003.13911. URL https://openaccess.thecvf.com/content_cvpr_2020/html/Kim_Proxy_Anchor_Loss_for_Deep_Metric_Learning_CVPR_2020_paper.html.
- Thomas N. Kipf and Max Welling. Semi-supervised classification with graph convolutional networks. In *International Conference on Learning Representations (ICLR)*, 2017. doi: 10.48550/arXiv.1609.02907.
- Alexander Lappe and Martin A. Giese. Register and [CLS] tokens induce a decoupling of local and global features in large ViTs. In *Advances in Neural Information Processing Systems (NeurIPS)*, 2025. URL <https://openreview.net/forum?id=Khavyz09kK>.
- Qingge Li, Xiaogang Yang, Jiwei Fan, Ruitao Lu, Bin Tang, Siyu Wang, and Shuang Su. GeoFormer: An effective Transformer-based Siamese network for UAV geolocalization. *IEEE Journal of Selected Topics in Applied Earth Observations and Remote Sensing*, 17:9470–9491, 2024. doi: 10.1109/JSTARS.2024.3392812.
- Jinliang Lin, Zhiming Luo, Dazhen Lin, Shaozi Li, and Zhun Zhong. A self-adaptive feature extraction method for aerial-view geo-localization. *IEEE Transactions on Image Processing*, 34: 126–139, 2025. doi: 10.1109/TIP.2024.3513157.
- Tsung-Yi Lin, Yin Cui, Serge Belongie, and James Hays. Learning deep representations for ground-to-aerial geolocalization. In *Proceedings of the IEEE Conference on Computer Vision and Pattern Recognition (CVPR)*, 2015. URL https://openaccess.thecvf.com/content_cvpr_2015/html/Lin_Learning_Deep_Representations_for_CVPR_2015_paper.html.
- Xiangzeng Liu, Ziyao Wang, Yue Wu, and Qiguang Miao. SeGCN: A semantic-aware graph convolutional network for UAV geo-localization. *IEEE Journal of Selected Topics in Applied Earth Observations and Remote Sensing*, 17:6055–6066, 2024. doi: 10.1109/JSTARS.2024.3370612.
- Francesco Locatello, Dirk Weissenborn, Thomas Unterthiner, Aravindh Mahendran, Georg Heigold, Jakob Uszkoreit, Alexey Dosovitskiy, and Thomas Kipf. Object-centric learning with slot attention. In *Advances in Neural Information Processing Systems (NeurIPS)*, 2020. doi: 10.48550/arXiv.2006.15055.
- Huashao Luo, Junwei Bao, Youzheng Wu, Xiaodong He, and Tianrui Li. SegCLIP: Patch aggregation with learnable centers for open-vocabulary semantic segmentation. In *Proceedings of the International Conference on Machine Learning (ICML)*, 2023. doi: 10.48550/arXiv.2211.14813.
- Zhe Ma, Jianfeng Dong, Shouling Ji, Zhenguang Liu, Xuhong Zhang, Zonghui Wang, Sifeng He, Feng Qian, Xiaobo Zhang, and Lei Yang. Let all be whitened: Multi-teacher distillation for efficient visual retrieval. In *Proceedings of the AAAI Conference on Artificial Intelligence*, volume 38, pages 5143–5151, 2024. URL <https://ojs.aaai.org/index.php/AAAI/article/view/28207/28410>.
- David Marr and H. Keith Nishihara. Representation and recognition of the spatial organization of three-dimensional shapes. *Proceedings of the Royal Society of London. Series B, Biological Sciences*, 200(1140):269–294, 1978. doi: 10.1098/rspb.1978.0020.

- Maxime Oquab, Timothée Darcet, Théo Moutakanni, Huy Vo, Marc Szafraniec, Vasil Khalidov, Pierre Fernandez, Daniel Haziza, Francisco Massa, Alaaeldin El-Nouby, et al. DINOv2: Learning robust visual features without supervision. *Transactions on Machine Learning Research*, 2024. URL <https://openreview.net/pdf?id=GLm1BA3C8p>.
- Wonpyo Park, Dongju Kim, Yan Lu, and Minsu Cho. Relational knowledge distillation. In *Proceedings of the IEEE/CVF Conference on Computer Vision and Pattern Recognition (CVPR)*, pages 3967–3976, 2019. URL https://openaccess.thecvf.com/content_CVPR_2019/papers/Park_Relational_Knowledge_Distillation_CVPR_2019_paper.pdf.
- Ethan Perez, Florian Strub, Harm de Vries, Vincent Dumoulin, and Aaron Courville. FiLM: Visual reasoning with a general conditioning layer. In *Proceedings of the AAAI Conference on Artificial Intelligence*, 2018. doi: 10.1609/aaai.v32i1.11671.
- Yifan Ping, Jun Lu, Haitao Guo, Qingfeng Hou, Kun Zhu, Zehao Sang, and Tong Liu. DINO-MSRA: A novel network architecture for cross-view image retrieval and localization of UAV and satellite images. *Journal of Geo-information Science*, 27(7):1608–1623, 2025. doi: 10.12082/dqxkx.2025.250051.
- Katarina Radoš, Marta Brkić, and Dinko Begušić. Recent advances on jamming and spoofing detection in GNSS. *Sensors*, 24(13):4210, 2024. doi: 10.3390/s24134210.
- Florian Schroff, Dmitry Kalenichenko, and James Philbin. FaceNet: A unified embedding for face recognition and clustering. In *Proceedings of the IEEE Conference on Computer Vision and Pattern Recognition (CVPR)*, 2015. doi: 10.1109/CVPR.2015.7298682. URL <https://ieeexplore.ieee.org/document/7298682>.
- Ozan Sener and Vladlen Koltun. Multi-task learning as multi-objective optimization. In *Advances in Neural Information Processing Systems (NeurIPS)*, 2018. doi: 10.48550/arXiv.1810.04650.
- Tianrui Shen, Yingmei Wei, Lai Kang, Shanshan Wan, and Yee-Hong Yang. MCCG: A ConvNeXt-based multiple-classifier method for cross-view geo-localization. *IEEE Transactions on Circuits and Systems for Video Technology*, 34(3):1456–1468, 2024. doi: 10.1109/TCSVT.2023.3296074.
- Yujiao Shi, Xin Yu, Dylan Campbell, and Hongdong Li. Where am I looking at? Joint location and orientation estimation by cross-view matching. In *Proceedings of the IEEE/CVF Conference on Computer Vision and Pattern Recognition (CVPR)*, 2020. URL https://openaccess.thecvf.com/content_CVPR_2020/html/Shi_Where_Am_I_Looking_At_Joint_Location_and_Orientation_Estimation_CVPR_2020_paper.html.
- Jian Sun, Hao Sun, Lin Lei, Kefeng Ji, and Gangyao Kuang. TirSA: A three stage approach for UAV-satellite cross-view geo-localization based on self-supervised feature enhancement. *IEEE Transactions on Circuits and Systems for Video Technology*, 34(9):7882–7895, 2024. doi: 10.1109/TCSVT.2024.3382717.
- Yifan Sun, Liang Zheng, Yi Yang, Qi Tian, and Shengjin Wang. Beyond part models: Person retrieval with refined part pooling (and a strong convolutional baseline). In *Proceedings of the European Conference on Computer Vision (ECCV)*, 2018. URL https://openaccess.thecvf.com/content_ECCV_2018/html/Yifan_Sun_Beyond_Part_Models_ECCV_2018_paper.html.
- Yifan Sun, Changmao Cheng, Yuhan Zhang, Chi Zhang, Liang Zheng, Zhongdao Wang, and Yichen Wei. Circle loss: A unified perspective of pair similarity optimization. In *Proceedings of the IEEE/CVF Conference on Computer Vision and Pattern Recognition (CVPR)*, 2020. doi: 10.1109/CVPR42600.2020.00643. URL https://openaccess.thecvf.com/content_CVPR_2020/html/Sun_Circle_Loss_A_Unified_Perspective_of_Pair_Similarity_Optimization_CVPR_2020_paper.html.
- Antti Tarvainen and Harri Valpola. Mean teachers are better role models: Weight-averaged consistency targets improve semi-supervised deep learning results. In *Advances in Neural Information Processing Systems (NeurIPS)*, 2017. URL <https://proceedings.neurips.cc/paper/2017/hash/5a61e2356a4a14f2a8c4e1a4c4c7e26a-Abstract.html>.
- Yonglong Tian, Dilip Krishnan, and Phillip Isola. Contrastive representation distillation. In *International Conference on Learning Representations (ICLR)*, 2020. URL <https://openreview.net/pdf?id=SkgpBJrtvS>.

- Aäron van den Oord, Yazhe Li, and Oriol Vinyals. Representation learning with contrastive predictive coding. In *Advances in Neural Information Processing Systems (NeurIPS)*, 2018. doi: 10.48550/arXiv.1807.03748.
- Ashish Vaswani, Noam Shazeer, Niki Parmar, Jakob Uszkoreit, Llion Jones, Aidan N. Gomez, Lukasz Kaiser, and Illia Polosukhin. Attention is all you need. In *Advances in Neural Information Processing Systems (NeurIPS)*, 2017. URL <https://proceedings.neurips.cc/paper/2017/hash/3f5ee243547dee91fbd053c1c4a845aa-Abstract.html>.
- Petar Veličković, Guillem Cucurull, Arantxa Casanova, Adriana Romero, Pietro Liò, and Yoshua Bengio. Graph attention networks. In *Proceedings of the International Conference on Learning Representations (ICLR)*, 2018. doi: 10.48550/arXiv.1710.10903. URL <https://openreview.net/forum?id=rJXmpikCZ>.
- Dequan Wang, Evan Shelhamer, Shaoteng Liu, Bruno Olshausen, and Trevor Darrell. Tent: Fully test-time adaptation by entropy minimization. In *Proceedings of the International Conference on Learning Representations (ICLR)*, 2021. doi: 10.48550/arXiv.2006.10726.
- Tingyu Wang, Zhedong Zheng, Chenggang Yan, Jiyong Zhang, Yaoqi Sun, Bolun Zheng, and Yi Yang. Each part matters: Local patterns facilitate cross-view geo-localization. *IEEE Transactions on Circuits and Systems for Video Technology*, 32(2):867–879, 2022. doi: 10.1109/TCSVT.2021.3061265.
- Tingyu Wang, Zhedong Zheng, Yaoqi Sun, Chenggang Yan, Yi Yang, and Tat-Seng Chua. Multiple-environment self-adaptive network for aerial-view geo-localization. *Pattern Recognition*, 152: 110363, 2024. doi: 10.1016/j.patcog.2024.110363.
- Tongzhou Wang and Phillip Isola. Understanding contrastive representation learning through alignment and uniformity on the hypersphere. In *International Conference on Machine Learning (ICML)*, 2020. doi: 10.48550/arXiv.2005.10242.
- Jiahao Wen, Hang Yu, and Zhedong Zheng. Weatherprompt: Multi-modality representation learning for all-weather drone visual geo-localization. In *Advances in Neural Information Processing Systems (NeurIPS)*, 2025. URL <https://nips.cc/virtual/2025/poster/118002>.
- Scott Workman, Richard Souvenir, and Nathan Jacobs. Wide-area image geolocalization with aerial reference imagery. In *Proceedings of the IEEE International Conference on Computer Vision (ICCV)*, 2015. URL https://openaccess.thecvf.com/content_iccv_2015/html/Workman_Wide-Area_Image_Geolocalization_ICCV_2015_paper.html.
- Qiong Wu, Yi Wan, Zhi Zheng, Yongjun Zhang, Guangshuai Wang, and Zhenyang Zhao. CAMP: A cross-view geo-localization method using contrastive attributes mining and position-aware partitioning. *IEEE Transactions on Geoscience and Remote Sensing*, 62:1–14, 2024. doi: 10.1109/TGRS.2024.3448499.
- Panwang Xia, Yi Wan, Zhi Zheng, Yongjun Zhang, and Jiwei Deng. Enhancing cross-view geo-localization with domain alignment and scene consistency. *IEEE Transactions on Circuits and Systems for Video Technology*, 34(12):13271–13281, 2024. doi: 10.1109/TCSVT.2024.3443510.
- Jin Xu, Junping Yin, Juan Zhang, and Tianyan Gao. Enhancing cross view geo localization through global local quadrant interaction network. *Scientific Reports*, 15:33431, 2025a. doi: 10.1038/s41598-025-18935-6.
- Yuanze Xu, Ming Dai, Wenxiao Cai, and Wankou Yang. Precise gps-denied uav self-positioning via context-enhanced cross-view geo-localization. In *Chinese Conference on Pattern Recognition and Computer Vision (PRCV)*, pages 374–388. Springer, 2025b. doi: 10.1007/978-981-95-5628-1_26.
- Jiaqiang Yang, Danyang Qin, Huapeng Tang, Sili Tao, Haoze Bie, and Lin Ma. DINOv2-based UAV visual self-localization in low-altitude urban environments. *IEEE Robotics and Automation Letters*, 10(2):2080–2087, 2025. doi: 10.1109/LRA.2025.3527762.
- Yibin Ye, Xichao Teng, Shuo Chen, Zhang Li, Leqi Liu, Qifeng Yu, and Tao Tan. Exploring the best way for UAV visual localization under low-altitude multi-view observation condition: A benchmark. In *Findings of the IEEE/CVF Conference on Computer Vision and Pattern Recognition (CVPR)*, 2026. doi: 10.48550/arXiv.2503.10692.

- Zhedong Zheng, Yunchao Wei, and Yi Yang. University-1652: A multi-view multi-source benchmark for drone-based geo-localization. In *Proceedings of the 28th ACM International Conference on Multimedia (ACM MM)*, pages 1395–1403, 2020. doi: 10.1145/3394171.3413896.
- Jinghao Zhou, Chen Wei, Huiyu Wang, Wei Shen, Cihang Xie, Alan Yuille, and Tao Kong. iBOT: Image BERT pre-training with online tokenizer. In *Proceedings of the International Conference on Learning Representations (ICLR)*, 2022. URL <https://openreview.net/pdf?id=ydopy-e6Dg>.
- Runzhe Zhu, Ling Yin, Mingze Yang, Fei Wu, Yuncheng Yang, and Wenbo Hu. SUES-200: A multi-height multi-scene cross-view image benchmark across drone and satellite. *IEEE Transactions on Circuits and Systems for Video Technology*, 33(9):4825–4839, 2023. doi: 10.1109/TCSVT.2023.3249204.

Appendix Contents

A1 Method Details	17
A1.1 Symbol Reference	17
A1.2 Theoretical Motivation: Formal Arguments	17
A1.3 Part-Head Mechanics, Masked Part Reconstruction, and Multi-Level Distillation . .	18
A1.4 UAPA: Formulation and Forward-KL Ablation	19
A1.5 GeoPartLoss Grouping and Training Details	20
A2 Implementation and Protocol	20
A2.1 Hyperparameter Configuration	20
A2.2 Dataset Statistics and Evaluation Protocol	20
A3 Extended Quantitative Results	20
A3.1 University-1652 Directional Comparison	20
A3.2 DenseUAV Detailed Comparison	20
A3.3 Backbone Ablation	21
A3.4 Weather Robustness: Full Protocol & Implementation	23
A3.5 Zero-shot Cross-Dataset Transfer	25
A3.6 Additional Pareto Analysis	25
A4 Qualitative Analysis and Discussion	26
A4.1 Qualitative Visualizations	26
A4.2 Limitations and Broader Impact	27
A4.3 What We Tried That Did Not Work	27

All SKYPART numbers follow the same single-pass evaluation protocol used in the main paper; reported baselines follow the source protocols stated in the corresponding tables.

A1 Method Details

A1.1 Symbol Reference

Table 5: Key symbols and their corresponding modules.

Symbol	Module	Section
\mathbf{P}, \mathbf{p}_k	Prototype bank: $K_{\max}=12$ slots (architectural ceiling), $d_p=256$; the saliency gate selects a per-image active subset of typical size $K=10$	3.2
$\mathbf{A}_{i,k}$	Soft assignment matrix	3.2
$\hat{\mathbf{p}}_k$	Part-aggregated features	3.2
g_k	Per-prototype saliency gate (Eq. 5)	A1.3
w_p, w_c, w_g	Three-way fusion weights (Eq. 2)	3.2
γ_a, β_a	FiLM scale & shift	3.3
\mathcal{L}_{mar}	Masked Part Reconstruction	A1.3
$\mathcal{L}_{\text{proxy}}$	Proxy Anchor loss	3.4
$\mathcal{L}_{\text{uapa}}$	Uncertainty-aware proxy alignment	3.4
\mathcal{L}_{div}	Prototype diversity regularizer	3.4
s_g	GeoPartLoss learnable log-variance	3.4

A1.2 Theoretical Motivation: Formal Arguments

The four framing choices of Sec. 3.1—an identity/arrangement factorization of the retrieval embedding, a softmax-over-prototype-indices assignment, altitude as a training-time nuisance, and uncertainty-weighted multi-task training—are reported there as a compressed narrative. This section expands each into a formal argument. None of the results below are claims of mathematical novelty; they are restatements of established theorems [Achille and Soatto, 2018, Locatello et al., 2020, Perez et al., 2018, Kendall et al., 2018, Sener and Koltun, 2018] applied to the CVGL setting. For convenience, we label the four arguments C1 (layout as sufficient statistic), C2 (slot-competition assignment), C3 (altitude as marginalized nuisance), and C4 (Pareto-stationary MTL).

C1 as an information-bottleneck factorization. Let X_d, X_s be drone and satellite views of the same scene with geolocation identity Y , and let $N = (N_{\text{view}}, N_{\text{alt}}, N_{\text{weather}})$ be the jointly observed nuisances. Write the CVGL retrieval embedding as $T = f_{\theta}(X)$. The information bottleneck objective [Achille and Soatto, 2018] asks for

$$\min_{\theta} I(T; X) - \beta I(T; Y), \quad (3)$$

with a separate *invariance* term $I(T; N) \rightarrow 0$. Factorize $T = (T_{\text{id}}, T_{\text{arr}})$ where T_{id} is the part-identity descriptor (drone’s part bank encoding) and T_{arr} is the part-arrangement descriptor (graph readout over prototype nodes). Two elementary observations motivate the split: (i) the part-arrangement statistic is approximately invariant to N_{view} (spatial layout of roads/roofs is preserved under oblique reprojection of a single planar scene) and to N_{weather} (weather destroys local texture but preserves spatial structure), so $I(T_{\text{arr}}; N) \ll I(T_{\text{id}}; N)$; (ii) T_{arr} alone is insufficient—two disjoint locations can share the same layout, so $I(T_{\text{arr}}; Y) < I(T; Y)$ and T_{id} must remain in the embedding. The three-branch fusion $\mathbf{f} = w_p \mathbf{f}_{\text{part}} + w_c \mathbf{f}_{\text{cls}} + w_g \mathbf{f}_{\text{graph}}$ is then exactly a learned linear combination of an identity-heavy component ($\mathbf{f}_{\text{part}}, \mathbf{f}_{\text{cls}}$) and an arrangement-heavy component ($\mathbf{f}_{\text{graph}}$), with the weights w_p, w_c, w_g learned end-to-end under the alignment objective. Empirically, the *No-Graph* ablation (Table 4, Block B) costs 1.17 pp Mean R@1 but 1.80 pp on Fog+Snow—the gap widens exactly in the regime where T_{id} ’s texture component is corrupted and the factorization is forced to rely on T_{arr} .

C2 as a single-pass slot assignment. Slot attention [Locatello et al., 2020] iterates an attention-then-GRU update for K slots competing over L input tokens. The competition comes from a softmax *across slots* (not across tokens), producing mutually-exclusive assignments that concentrate each token on one slot. Our single-pass assignment (Eq. 1) is the fixed point of one such iteration when (a) the slot-to-input similarity is parametrized as cosine with temperature τ , (b) the GRU update reduces

to identity, and (c) the slot initialization is the learned prototype bank rather than a sampled noise. In return for dropping the iterative refinement we lose a reconstruction-consistent slot assignment-but we do not need one. The downstream loss is not reconstruction; it is cross-view retrieval, for which a single competitive assignment is a sufficient statistic. The cost we pay is architectural: prototypes must be *learnable and directly trained*, rather than emerging from reconstruction pressure.

C3 as nuisance marginalization via FiLM mean. FiLM applies an affine modulation $\text{FiLM}(\mathbf{z}; \gamma_a, \beta_a) = \gamma_a \odot \mathbf{z} + \beta_a$ conditioned on an altitude bin $a \in A$. At inference, when altitude is unknown we replace (γ_a, β_a) with $(\bar{\gamma}, \bar{\beta}) = \frac{1}{|A|} \sum_a (\gamma_a, \beta_a)$. Under a uniform prior $p(a)$ this is exactly the expectation $\mathbb{E}_{a \sim p(a)} [\text{FiLM}(\mathbf{z}; \gamma_a, \beta_a)]$, the marginalized modulation. Because FiLM is linear in (γ_a, β_a) , the marginal is exactly the modulation produced by the marginal parameters *at the FiLM-operator output*. This equality is exact only at the affine modulation step; we do not claim the final fused embedding equals the marginal of the altitude-conditioned embedding, since downstream nonlinear layers (assignment softmax, GAT, fusion gate) break linearity. With this scope, the mean-FiLM fallback is a theoretically grounded substitution at the modulation operator rather than an ad-hoc hack. Conditioning the retrieval embedding directly on a (rather than conditioning only the clustering pathway and letting the final embedding collapse the altitude dimension through fusion) would instead make the embedding altitude-dependent at inference, which fails the deployment constraint motivated in Sec. 3.1.

C4 as Pareto-stationary MTL. Let $\{\mathcal{L}_g\}_{g=1}^G$ be the four group losses. Kendall homoscedastic uncertainty weighting [Kendall et al., 2018] models each task as a Gaussian likelihood with learned variance σ_g^2 : the log-likelihood contributes $\frac{1}{2\sigma_g^2} \mathcal{L}_g + \frac{1}{2} \log \sigma_g^2$, which after the reparameterization $s_g = \log \sigma_g^2$ becomes $\frac{1}{2} \exp(-s_g) \mathcal{L}_g + \frac{1}{2} s_g$. We adopt the equivalent form that drops the factor of $\frac{1}{2}$ (absorbed into the learning rate),

$$\mathcal{L}_{\text{total}} = \sum_g [\exp(-s_g) \mathcal{L}_g + s_g], \quad (4)$$

which is what Sec. 3.4 refers to as Eq. 4. Sener & Koltun [Sener and Koltun, 2018] prove that any stationary point of a non-negative weighted sum $\sum_g \alpha_g \mathcal{L}_g$ with $\alpha_g \geq 0$ and $\sum_g \alpha_g > 0$ is a Pareto-stationary point of the vector objective $(\mathcal{L}_1, \dots, \mathcal{L}_G)$: there is no descent direction that improves all \mathcal{L}_g simultaneously. Eq. 4 produces positive weights $\alpha_g = \exp(-s_g)$ by construction, so its stationary points inherit Pareto-stationarity. The log-variance term s_g prevents $\alpha_g \rightarrow \infty$ (the trivial collapse onto one task), and the learned values (alignment 0.94, distillation 1.05, part 1.12, altitude 1.18; Sec. 3.4) land in a tight range—a diagnostic that no single task is dominating. We do not claim that Pareto-stationarity is equivalent to Pareto-optimality; we claim only that Eq. 4 removes a four-dimensional weight sweep and replaces it with a stationarity property that follows from [Sener and Koltun, 2018].

Why these four, and why not more. A reader may ask why SKYPART does not additionally commit to, e.g., an equivariant backbone or an explicit nuisance adversary. Both are in the prior-art space ([Cohen and Welling, 2016, Ganin and Lempitsky, 2015]); we omitted both by design. Equivariance would bake a fixed rotation/scale prior into the backbone, but CVGL altitude/rotation distributions are dataset-specific (SUES-200 canonically oriented, DenseUAV arbitrary)—a fixed prior helps one and hurts the other. A domain-adversarial branch would couple training stability to a minimax game we explicitly want to avoid, given the Pareto-stationarity argument above. C1–C4 are the minimal set that determined our design; we do not claim they are the only reasonable set.

A1.3 Part-Head Mechanics, Masked Part Reconstruction, and Multi-Level Distillation

Saliency gate and active-set selection. The per-image saliency gate of Sec. 3.2 selects which prototypes are active for a given image. It is a Gumbel-sigmoid relaxation over per-prototype logits $\mathbf{s} \in \mathbb{R}^{K_{\text{max}}}$ computed from the part-aggregated descriptors $\hat{\mathbf{p}}_k$ (post-refine; the same tensor used by the graph readout and MAR) via a lightweight 2-layer MLP, $s_k = \text{MLP}_g(\hat{\mathbf{p}}_k)$ with hidden width $d_p/4=64$, GELU activation, and final-bias initialized to $b_2=2.0$ so the gate starts biased open ($\sigma(2.0) \approx 0.88$) and learns to prune:

$$g_k = \sigma((s_k + \epsilon_k)/\tau_g), \quad \epsilon_k \sim \text{Gumbel}(0, 1), \quad (5)$$

with $\tau_g=0.5$. A floor $K_{\min}=4$ is enforced at training time to prevent the gate from collapsing to a single prototype early. Each active prototype aggregates its assigned patch tokens through the soft assignment \mathbf{A} , passes through a small residual MLP, and its coordinate-normalized centroid in $[0, 1]^2$ is retained as the node position for the graph readout; this 2-D position is fed to the GAT as a node feature alongside the part descriptor, letting the layout readout depend on spatial relations between prototypes, not just their identities.

Per-branch projections to the fusion space. The three branches in Eq. 2 are projected to a shared 768-D space before the fusion gate combines them. (i) The CLS branch maps the 384-D DINOv2 ViT-S/14 CLS token through $\mathbf{f}_{\text{cls}} = \text{ReLU}(\text{BN}(W_c \text{CLS}))$ with $W_c \in \mathbb{R}^{768 \times 384}$. (ii) The part branch passes each of the K active 256-D part descriptors $\hat{\mathbf{p}}_k$ (post-refine, salience-weighted) through PartAwarePooling: it concatenates the top-3 part descriptors into a $3 \times 256=768$ vector and applies a 2-layer MLP $\mathbb{R}^{768} \rightarrow \mathbb{R}^{768}$ (Linear, LayerNorm, GELU, Linear) to produce \mathbf{f}_{part} . (iii) The graph branch projects the 256-D GAT readout \mathbf{h}_{GAT} through $\mathbf{f}_{\text{graph}} = \text{LN}(W_g \mathbf{h}_{\text{GAT}})$ with $W_g \in \mathbb{R}^{768 \times 256}$. The fusion gate’s MLP is $\mathbb{R}^{3 \cdot 768} \rightarrow \mathbb{R}^{384} \rightarrow \mathbb{R}^3$, followed by softmax. All three branch outputs are L2-normalized prior to the weighted sum.

Masked Part Reconstruction (MAR). 30% of patch tokens are masked; each masked position i is reconstructed through the part-aggregated features:

$$\mathcal{L}_{\text{mar}} = \frac{1}{|\mathcal{M}|} \sum_{i \in \mathcal{M}} (1 - \cos(\hat{\mathbf{z}}_i, \mathbf{z}_i)), \quad \hat{\mathbf{z}}_i = \text{Decoder}\left(\sum_k \mathbf{A}_{i,k} \hat{\mathbf{p}}_k\right), \quad (6)$$

where the decoder is a 2-layer MLP (GELU, LayerNorm, hidden size 512). Prototype aggregation $\hat{\mathbf{p}}_k$ uses only visible (unmasked) tokens, preventing target leakage. Soft assignments $\mathbf{A}_{i,k}$ at masked positions are detached (`stop_gradient`): without this, gradients flow back through assignment weights and one dominant prototype monopolizes all masked positions to trivially minimize \mathcal{L}_{mar} , bypassing diversity. The 30% mask ratio and 10-epoch warm-up balance reconstruction difficulty with optimization stability.

Multi-level distillation. We distill from a frozen DINOv2-B/14 teacher and an EMA self-ensemble, and regress the normalized ground-truth altitude $\tilde{a} = (a - 150)/150$, where a is the raw altitude in meters and \hat{a} denotes the prediction of the altitude regression head:

$$\mathcal{L}_{\text{cross}} = \text{MSE}(\phi \mathbf{f}, \mathbf{f}^T) + (1 - \cos(\phi \mathbf{f}, \mathbf{f}^T)), \quad (7)$$

$$\mathcal{L}_{\text{ema}} = 1 - \cos(\mathbf{f}, \mathbf{f}^{\text{ema}}) \quad (\alpha=0.996 \text{ [Tarvainen and Valpola, 2017]}), \quad (8)$$

$$\mathcal{L}_{\text{alt}} = \text{SmoothL1}(\hat{a}, \tilde{a}). \quad (9)$$

The teacher mapping ϕ is a lightweight projector $\phi(\mathbf{f}) = \text{LayerNorm}(\mathbf{W}\mathbf{f})$ with $\mathbf{W} \in \mathbb{R}^{768 \times 768}$ matching student to teacher dimensionality.

A1.4 UAPA: Formulation and Forward-KL Ablation

UAPA formulation. Let $\mathbf{p}_d, \mathbf{p}_s$ be the softmax probabilities over the $|C|$ proxy classes, with one proxy per training location ($|C|=120$ for SUES-200, 701 for University-1652, and 2,256 for DenseUAV). The proxy-classification head reuses the $|C|$ proxy embeddings from metric learning: each logit is the cosine similarity between the normalized retrieval embedding and a learned class proxy, followed by a softmax over the $|C|$ classes. Entropy is computed over these proxy-class probabilities.

UAPA modulates only the KL temperature using the positive relative entropy gap between the drone and satellite proxy distributions:

$$T = T_0(1 + \Delta H_+ / H_{\text{max}}), \quad \Delta H_+ = \max\{H(\mathbf{p}_d) - H(\mathbf{p}_s), 0\}, \quad (10)$$

where $H(\cdot)$ is Shannon entropy, $T_0=4$, and $H_{\text{max}} = \log |C|$ normalizes the entropy gap. Since $0 \leq \Delta H_+ \leq H_{\text{max}}$, the effective UAPA temperature lies in $[T_0, 2T_0] = [4, 8]$. When the drone view is more uncertain than the satellite view, T increases and softens the satellite-teacher target; otherwise the temperature remains at the base value. The loss itself is the standard temperature-softened reverse KL evaluated at T , $\mathcal{L}_{\text{uapa}} = T^2 \text{KL}(\text{softmax}(\mathbf{z}_d/T) \parallel \text{softmax}(\mathbf{z}_s/T))$, where $\mathbf{z}_d, \mathbf{z}_s$ are the proxy-class logits and the T^2 scaling preserves gradient magnitude across temperatures, so only the temperature (not a whole-sample re-weighting) is modulated.

KL direction. We use reverse KL (drone||satellite, mode-seeking) rather than forward KL (mode-covering), so the drone branch is encouraged to concentrate on the most confident satellite peak. A forward-KL variant plateaus at 96.52% R@1 versus 98.74% for reverse KL (-2.22 pp). GeoPartLoss group weights converge to similar ratios under either choice (alignment 0.97, distillation 1.01, part 1.03, altitude 1.04 for forward KL), suggesting that self-calibration is robust to the KL direction.

A1.5 GeoPartLoss Grouping and Training Details

Table 6: **GEOPARTLOSS groups** (aligned with implementation). Converged weights are end-of-training averages from the SUES-200 canonical run (60 epochs); higher $\exp(-s_g)$ = group receives stronger gradient.

Group	Constituent losses	Weighting	Converged $\exp(-s_g)$
Alignment	$\mathcal{L}_{\text{circle}} + \mathcal{L}_{\text{ncc}} + \mathcal{L}_{\text{proxy}} + \mathcal{L}_{\text{uapa}}$	$\exp(-s_{\text{align}})$	0.94
Distillation	$\mathcal{L}_{\text{cross}} + \mathcal{L}_{\text{ema}}$	$\exp(-s_{\text{distill}})$	1.05
Part quality	$\mathcal{L}_{\text{mar}} + \mathcal{L}_{\text{div}}$	$\exp(-s_{\text{part}})$	1.12
Altitude	\mathcal{L}_{alt}	$\exp(-s_{\text{alt}})$	1.18
Regularizer	$+\sum_g s_g$ (Kendall uncertainty)	automatic	—

The learned group weights $\exp(-s_g)$ evolve during training rather than collapsing to a fixed split: from uniform initialization they diverge within the first 20 epochs and settle by epoch 60 at approximately alignment 0.94, distillation 1.05, part quality 1.12, altitude 1.18. Alignment dominates early, when the embedding geometry is being established, and then relaxes as metric learning saturates while the part-quality and altitude weights rise to compensate-the behaviour Kendall weighting should show as harder objectives take over. The log-variance regularizer $+\sum_g s_g$ keeps all four groups from collapsing to zero so gradient flow stays healthy throughout the schedule. The diversity regularizer in the part-quality group penalises off-diagonal cosine similarities between L2-normalised prototypes, $\mathcal{L}_{\text{div}} = \frac{1}{K_{\text{max}}(K_{\text{max}}-1)} \sum_{j \neq k} \langle \mathbf{p}_j, \mathbf{p}_k \rangle^2$, pushing the bank toward an orthogonal (well-spread) set so different prototypes attend to genuinely different scene regions. The patch-level NCE term in the alignment group uses, as positives, patch pairs assigned to the same prototype in both views and, as negatives, all other patches in the batch; this is what allows the loss to remain well-defined when a prototype’s role drifts during training (see Appendix A4.2 on label equivariance).

A2 Implementation and Protocol

A2.1 Hyperparameter Configuration

Table 7 lists the complete set of hyperparameters. Values are frozen across all experiments and matched to the deployed training configuration.

A2.2 Dataset Statistics and Evaluation Protocol

Table 8 lists the train split sizes and the per-direction query/gallery counts used by all retrieval evaluations in the main paper.

A3 Extended Quantitative Results

A3.1 University-1652 Directional Comparison

Table 9 extends the main-paper Table 2(a) with a wider set of University-1652 baselines and reports both retrieval directions for each.

A3.2 DenseUAV Detailed Comparison

Table 10 extends the main-paper Table 2(b) with additional DenseUAV metrics (R@5, R@top1, AP, SDM@{1,3,5}) for the same set of baselines.

Table 7: Complete hyperparameter configuration.

Category	Parameter	Value
Architecture	Backbone	DINOv2 ViT-S/14
	Unfrozen blocks	6 (of 12)
	Prototype bank size K_{\max}	12
	Active prototype count K (typical)	10
	Part dimension d_p	256
	Embedding dim D	768
	Teacher dim	768
	Cluster temperature τ	0.07
Training	Input size	448×448
	Epochs	60
	PK sampler (P, M)	(16, 4)
	Head LR	3×10^{-4}
	Backbone LR	3×10^{-5}
	Weight decay	0.05
	Warmup epochs	5
	LR floor	1% of peak
Loss	Proxy margin δ	0.1
	Proxy scale α	32
	EMA decay α	0.996
	MAR mask ratio	0.30
	MAR warmup	10 epochs
	Distillation temp	4.0
	Num loss groups	4
	Label smoothing	0.1

Table 8: Training split sizes and test query/gallery counts for both retrieval directions on the three benchmarks.

Dataset	Training phase		Test phase			
	Drone	Satellite	Drone→Satellite		Satellite→Drone	
			Query	Gallery	Query	Gallery
University-1652 [Zheng et al., 2020]	37,854	701	37,855	951	701	51,355
SUES-200 [Zhu et al., 2023]	24,000	120	16,000	200	50	40,000
DenseUAV [Dai et al., 2024]	6,768	13,536	2,331	18,198	4,662	9,099

A3.3 Backbone Ablation

Table 11 reports a controlled *SSL ViT generalisation* ablation on SUES-200 with everything else held identical: resolution, loss grouping, augmentation recipe, optimizer, epoch budget, and confusion gallery. The same Full SKYPART head is attached to three ViT-S self-supervised backbones (DINOv2 [Oquab et al., 2024], iBOT [Zhou et al., 2022], MoCo v3 [Chen et al., 2021]) under a strictly matched 60-epoch budget with teacher distillation *disabled* (CLS-only baselines are 60 epochs, same recipe), so the head’s plug-and-play behaviour is read off the lift over each backbone’s own CLS-only rather than off absolute R@1. The deployed configuration (DINOv2 ViT-S/14 + Full head, 60 epochs, distillation *enabled*) is not retrained here; its headline number (Mean R@1 98.74% D→S) is the row in Table 1, and the DINOv2 row of Table 11 (98.48%) is the within-block SSL anchor only. We omit a ConvNeXt-T row because, in our pilot, the Full SKYPART head on ImageNet-supervised ConvNeXt-T regressed from 92.33% (CLS-only) to 90.41% Mean R@1 under the same 60-epoch recipe—a negative transfer consistent with the prototype-to-patch assignment requiring patch-level semantic coherence that emerges in self-distilled ViTs but not in supervised CNN feature maps. Per-altitude D→S and S→D R@1 are reported for each row.

The three SSL substrates tell a single story sharpened by the patch-token quality of each backbone. On the two self-distilled substrates (DINOv2, iBOT), CLS-only is already moderately strong (88.68 / 84.54% Mean D→S R@1), and the Full SKYPART head delivers a clean positive lift across all altitudes (+9.80 pp on DINOv2, +5.62 pp on iBOT)—the head adds usable layout structure on top

Table 9: **University-1652 directional comparison.** We report both retrieval directions, Drone→Satellite and Satellite→Drone, using R@1 and AP. “-” indicates values not reported in the cited papers/tables under the exact matched protocol. **Red**: best; **blue**: second-best.

Method	Venue	Params	Drone → Satellite		Satellite → Drone	
			R@1	AP	R@1	AP
ViT [Dosovitskiy et al., 2021]	ICLR’20	-	74.09	77.82	83.31	72.27
FSRA [Dai et al., 2022]	TCSVT’21	-	85.50	87.53	89.73	84.94
Swin-B	CVPR’21	-	84.15	86.62	90.30	83.55
LPN [Wang et al., 2022]	TCSVT’22	62.4M	77.71	80.80	90.30	78.78
RK-Net	TIP’22	-	68.10	71.53	80.96	69.35
SwinV2-B	CVPR’22	-	86.99	89.02	91.16	85.77
Sample4Geo (ResNet-50) [Deuser et al., 2023]	ICCV’23	-	78.62	82.11	87.45	76.32
Sample4Geo (ConvNeXt-B) [Deuser et al., 2023]	ICCV’23	87.6M	92.65	93.81	95.14	91.39
DenseUAV baseline [Dai et al., 2024]	TIP’23	-	82.22	84.78	87.59	81.49
F3-Net	TGRS’23	-	78.64	81.60	-	-
Song	GRSL’23	-	83.26	85.84	90.30	82.71
AEN (w. LPN)	SPL’24	-	77.40	80.27	90.30	76.01
MuSe-Net [Wang et al., 2024]	PR’24	50.5M	74.48	77.83	88.02	75.10
TransFG	TGRS’24	-	87.92	89.99	93.37	87.94
MFJRLN(Lcro) [Ge et al., 2024]	TGRS’24	-	87.61	89.57	91.07	86.72
GeoFormer [Li et al., 2024]	J-STARS’24	-	88.16	90.03	91.87	87.92
MCCG [Shen et al., 2024]	TCSVT’24	56.6M	89.28	91.01	94.29	89.29
SDPL [Chen et al., 2024]	TCSVT’24	-	90.16	91.64	93.58	89.45
CCR [Du et al., 2024]	TCSVT’24	156.6M	92.54	93.78	95.15	91.80
CAMP [Wu et al., 2024]	TGRS’24	91.0M	94.46	95.38	96.15	92.72
DAC [Xia et al., 2024]	TCSVT’24	96.5M	94.67	95.50	96.43	93.79
MEAN [Chen et al., 2025]	TGRS’25	36.5M	93.55	94.53	96.01	92.08
SKYPART (Ours)	-	26.95M	96.47	97.77	98.43	98.24

Table 10: **DenseUAV detailed comparison** with additional retrieval and SDM metrics. Top and second-best entries follow the same highlighting rule as the main tables. **Red**: best; **blue**: second.

Method	Venue	Backbone	R@1	R@5	R@top1	AP	SDM@1	SDM@3	SDM@5
Triplet Loss	CVPR’15	ResNet-50	11.88	32.22	-	-	21.91	-	-
Instance Loss	ACMMM’20	ResNet-50	13.00	35.78	-	-	23.61	-	-
LCM	Remote Sens’20	ResNet-50	25.37	50.92	-	-	35.52	-	-
MSBA	Remote Sens’21	ResNet-50	46.13	64.22	-	-	52.64	-	-
LPN (ResNet-50)	TCSVT’21	ResNet-50	32.43	56.80	-	-	40.26	-	-
LPN (ViT-S)	TCSVT’21	ViT-S	71.77	90.13	-	-	77.95	-	-
FSRA	TCSVT’21	ViT-S	81.21	94.55	99.89	71.93	85.11	83.54	79.74
RK-Net	TIP’22	ResNet-50	38.74	62.85	-	-	45.78	-	-
Sample4Geo	ICCV’23	ConvNeXt-B	49.38	78.29	99.40	35.93	61.72	-	-
DenseUAV baseline	TIP’23	ViT-S	83.01	95.58	99.91	72.10	86.50	84.50	80.44
MCCG	TCSVT’24	ConvNeXt-T	83.14	93.39	99.74	72.60	85.94	84.32	80.14
Yang et al.	RA-L’25	DINOv2-B	86.27	96.83	-	-	88.87	-	-
CEUSP	PRCV’25	ConvNeXt-T	89.45	96.05	100.00	79.62	91.01	89.42	85.34
SKYPART (Ours)	-	DINOv2-S	91.85	97.81	99.61	92.52	93.59	92.40	79.33

of an already coherent patch grid, and the deployed 98.74% Mean R@1 on D→S (Table 1) comes from combining this DINOv2 patch substrate with the teacher-distillation pathway that this ablation deliberately strips out. On the contrastive substrate (MoCo v3), CLS-only collapses to 28.19% Mean R@1 because contrastive pretraining optimises the CLS slot but leaves patch tokens diffuse; the Full SKYPART head recovers the structural signal that the patch-affinity graph and prototype assignment can read out and lifts D→S Mean R@1 by +33.49 pp (and S→D Mean R@1 by +31.88 pp). Combined with the negative-transfer outcome on ImageNet-supervised ConvNeXt-T noted in the intro, the picture is consistent: SKYPART’s contribution is *architectural* (it activates the latent layout signal that any patch-token SSL ViT exposes), and the magnitude of the lift scales inversely with how much of that signal the global CLS slot has already captured.

Table 11: **Backbone generalisation on SUES-200** (Normal weather, single-scale 448×448 , full 200-tile gallery, no re-ranking, no TTA). We compare self-supervised ViT backbones under a controlled setting (Full = 60 epochs, teacher distillation disabled; CLS-only baseline = 60 epochs with the same recipe). The proposed head transfers cleanly between self-distilled patch substrates (DINOv2, iBOT) and provides a large lift on the contrastive MoCo v3 substrate, whose CLS embedding is substantially weaker for dense retrieval. The deployed SKYPART model, trained for 60 epochs with teacher distillation enabled, is reported as the headline result.

Backbone	Head	Drone \rightarrow Satellite, R@1 (%)					Satellite \rightarrow Drone, R@1 (%)				
		150m	200m	250m	300m	Mean	150m	200m	250m	300m	Mean
DINOv2 ViT-S/14	CLS-only	82.20	88.08	91.80	92.65	88.68	97.50	93.75	97.50	96.25	96.25
DINOv2 ViT-S/14	Full SKYPART	96.25	98.75	99.30	99.60	98.48	100.00	100.00	100.00	100.00	100.00
	Δ vs CLS	+14.05	+10.67	+7.50	+6.95	+9.80	+2.50	+6.25	+2.50	+3.75	+3.75
iBOT ViT-S/16	CLS-only	73.80	85.40	88.75	90.20	84.54	88.75	91.25	92.50	93.75	91.56
iBOT ViT-S/16	Full SKYPART	82.43	91.10	93.63	93.50	90.16	96.25	97.50	97.50	97.50	97.19
	Δ vs CLS	+8.63	+5.70	+4.88	+3.30	+5.62	+7.50	+6.25	+5.00	+3.75	+5.63
MoCo v3 ViT-S/16	CLS-only	20.90	28.55	31.85	31.48	28.19	36.25	50.00	55.00	58.75	50.00
MoCo v3 ViT-S/16	Full SKYPART	48.25	61.80	66.98	69.68	61.68	71.25	82.50	87.50	86.25	81.88
	Δ vs CLS	+27.35	+33.25	+35.13	+38.20	+33.49	+35.00	+32.50	+32.50	+27.50	+31.88

A3.4 Weather Robustness: Full Protocol & Implementation

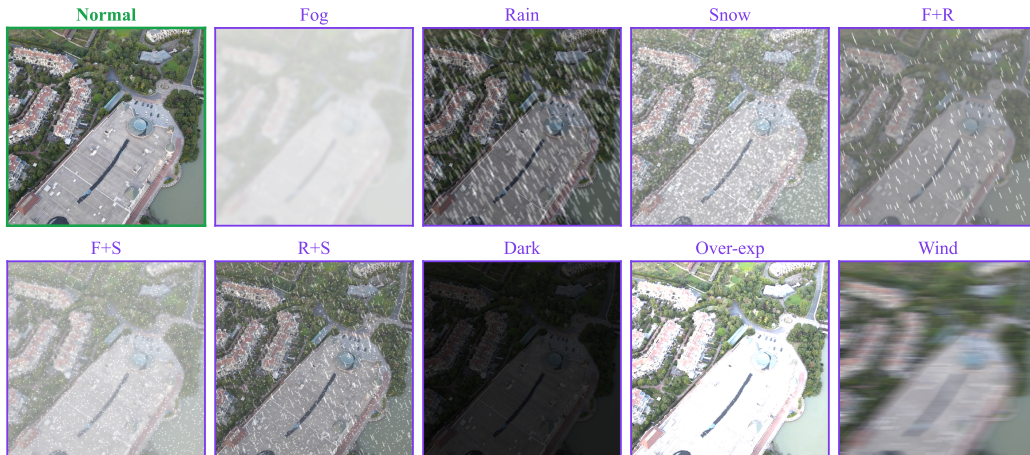


Figure 3: **Weather conditions.** The same drone image under 10 WeatherPrompt augmentations. Texture is destroyed, but spatial structure persists—a pattern qualitatively aligned with layout-heavy representations and with SKYPART’s relative robustness under environmental noise.

A3.4.1 Evaluation Protocol

The evaluation protocol follows the WeatherPrompt guidelines: the satellite gallery remains clean while drone queries are corrupted on-the-fly (Fig. 3), testing generalization to adversarial conditions without access to weather-augmented satellite data. Evaluation spans ten conditions—individual effects (fog, rain, snow, darkness, over-exposure, wind) and three pairwise combinations (fog+rain, fog+snow, rain+snow)—using Recall and mean Average Precision as standard metrics. Per-condition robustness across the three benchmarks is summarized in Fig. 4.

A3.4.2 Weather Augmentation Implementation

All augmentations use identical `imgaug` parameters as the WeatherPrompt source code (Table 12). We apply this corruption pipeline to SKYPART on all three datasets, and to the DenseUAV baselines that we retrained end-to-end (no published WeatherPrompt numbers exist for DenseUAV); SUES-200 and University-1652 baselines are taken directly from WeatherPrompt at their published 384×384 resolution and are not re-trained, while SKYPART is fine-tuned at 392×392 ; the full per-block recipe (clean retrieval, DenseUAV weather fine-tune, SUES-200/University-1652 weather) is summarized

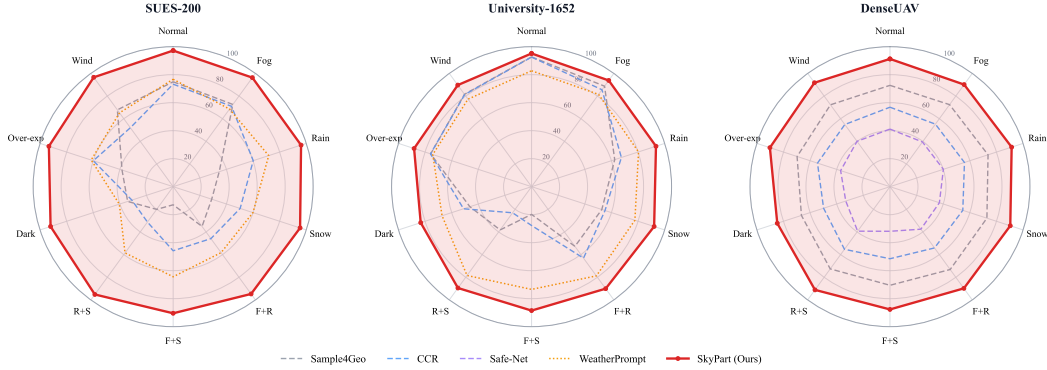


Figure 4: **Weather robustness across three benchmarks (radar view).** Per-condition Drone→Satellite R@1 (%) under the ten WeatherPrompt corruptions on SUES-200, University-1652, and DenseUAV. SKYPART (red, filled) maintains a near-circular profile, indicating uniform robustness across all conditions, while baselines collapse on hard regimes (F+S, Dark). Numerical breakdown matches Table 3.

in Table 13. **Resolution and retraining scope.** On SUES-200 and University-1652, baselines are reported from WeatherPrompt at their native 384×384 because their ConvNeXt-B / supervised-ViT backbones lock that resolution (positional encodings degrade if forcibly retrained off-spec), while SKYPART is trained at 392×392 to yield a full 28×28 patch grid for DINOv2 ViT-S/14; the SUES-200 / University-1652 weather numbers should be read as reported-baseline at each method’s published resolution rather than fully resolution-controlled, as marked in the caption of Table 3. On DenseUAV (no published WeatherPrompt baselines), all methods including SKYPART are retrained end-to-end under one shared recipe: same 60-epoch schedule, identical imgaug seeds (fixed per batch), each method at its own native input resolution, and the official full DenseUAV gallery. The three seeds (42, 123, 2024) used for the main SUES-200 result are re-used for each DenseUAV baseline; across baselines, R@1 variance is under 0.4 pp seed-to-seed. Weather-condition sampling is uniform per batch (10 conditions). Augmentation seeds are released with the training scripts so retraining any method under an exactly matched regimen is reproducible end-to-end.

Table 12: Weather augmentation parameters (identical to WeatherPrompt).

Condition	imgaug Augmenter	Parameters
Normal	<code>iaa.Identity()</code>	-
Fog	<code>iaa.Fog()</code>	Default parameters
Rain	<code>iaa.Rain()</code>	<code>speed=(0.1, 0.3)</code>
Snow	<code>iaa.Snowflakes()</code>	<code>flake_size=(0.1, 0.4), speed=(0.01, 0.05)</code>
Dark	<code>iaa.Multiply()</code>	<code>(0.3, 0.5)</code>
Light	<code>iaa.Multiply()</code>	<code>(1.5, 2.0)</code>
Fog+Rain	<code>Sequential([Fog, Rain])</code>	Same as individual
Fog+Snow	<code>Sequential([Fog, Snow])</code>	Same as individual
Rain+Snow	<code>Sequential([Rain, Snow])</code>	Same as individual
Wind	<code>iaa.MotionBlur()</code>	<code>k=15, angle=[-45, 45]</code>

A3.4.3 Training Setup (Fine-tuning)

For robustness experiments, baseline numbers are taken from WeatherPrompt [Wen et al., 2025] at their reported configuration; SKYPART is fine-tuned for 60 epochs on SUES-200 at 392×392 under a matched optimizer, batch size, and schedule. Weather augmentations are applied online to the drone images only, while the satellite view remains clean, and all ten conditions are sampled uniformly per batch. For DenseUAV, we use the same optimizer (AdamW), batch size, and cosine learning-rate schedule across all retrained methods, scaling the base learning rate down by a factor of 0.3 relative to clean training to stabilize adaptation. This matched DenseUAV schedule ensures that SKYPART’s weather gains there reflect its part-centric design rather than extra training budget; for SUES-200 and University-1652, the comparison should be read as reported-baseline (Table 3 caption).

Table 13: **Experiment recipes across all reported results.** We use two distinct configurations: a *clean* config at 448×448 for the main retrieval tables (SUES-200, University-1652, DenseUAV) and a *weather* config at 392×392 for WeatherPrompt evaluation. For the DenseUAV weather block all baselines are retrained end-to-end with AdamW, cosine LR, 60 epochs, and identical imgaug augmentations; for SUES-200 and University-1652 weather, baselines are reported from WeatherPrompt [Wen et al., 2025] at their published configuration and SKYPART is evaluated under the same corruption pipeline at 392×392 (resolution and budget differences are explicit in the rows below).

Result block	Method	Backbone	Res.	Epochs	Base LR	Batch
<i>Clean retrieval</i> (Tables 1, 2; single-pass, no re-ranking, no TTA)						
SUES-200 / Uni-1652 / DenseUAV	SKYPART (deployed)	DINOv2-S	448×448	60	3×10^{-4}	64
<i>Weather fine-tune—DenseUAV</i> (all baselines retrained end-to-end; Table 16)						
DenseUAV-W	Sample4Geo [Deuser et al., 2023]	ConvNeXt-B	384×384	60	3×10^{-5}	64
DenseUAV-W	Safe-Net [Lin et al., 2025]	ResNet-50	256×256	60	1×10^{-4}	64
DenseUAV-W	CCR [Du et al., 2024]	ConvNeXt-B	384×384	60	3×10^{-5}	64
DenseUAV-W	WeatherPrompt [Wen et al., 2025]	ConvNeXt-B	384×384	60	3×10^{-5}	64
DenseUAV-W	SKYPART (fine-tune)	DINOv2-S	392×392	60	1×10^{-4}	64
<i>Weather—SUES-200 / University-1652</i> (Tables 14, 15)						
SUES/Uni	WeatherPrompt baselines [Wen et al., 2025]	ConvNeXt-B	384×384	as published (reported-baseline)		
SUES/Uni	SKYPART (fine-tune)	DINOv2-S	392×392	60	1×10^{-4}	64

Table 14: **Full WeatherPrompt robustness on SUES-200.** Per-condition R@1/AP (%) for both $D \rightarrow S$ and $S \rightarrow D$. Baselines are reported from WeatherPrompt [Wen et al., 2025]; SKYPART is evaluated under the same corruption pipeline at 392×392 . This is the detailed SUES-200 version summarized in Table 3. **Red**: best; **blue**: second.

Method	Clean		Fog		Rain		Snow		F+R		F+S		R+S		Dark		Over-exp		Wind		Mean	
	R@1	AP	R@1	AP	R@1	AP	R@1	AP	R@1	AP	R@1	AP	R@1	AP	R@1	AP	R@1	AP	R@1	AP	R@1	AP
Drone \rightarrow Satellite																						
Zheng et al. [Zheng et al., 2020]	57.70	58.30	48.63	49.61	53.41	52.72	41.78	43.47	37.17	37.44	44.22	46.18	40.60	40.63	23.81	25.45	49.79	50.64	47.42	48.31	44.43	45.12
IBN-Net	65.34	63.78	56.03	56.57	55.73	58.55	47.80	49.53	43.45	44.98	50.04	51.00	45.51	45.92	29.61	30.93	56.01	56.96	57.36	58.10	50.69	51.63
Sample4Geo [Deuser et al., 2023]	74.93	78.76	72.58	76.44	34.60	41.56	28.95	35.02	35.10	41.47	12.95	17.90	20.05	25.95	34.18	38.99	38.40	43.68	67.80	72.41	41.95	47.22
Safe-Net [Lin et al., 2025]	76.31	75.35	73.53	73.44	54.15	55.05	48.94	50.10	45.12	47.92	40.05	40.18	25.95	26.12	29.74	31.48	54.86	58.68	58.10	58.95	50.68	51.63
CCR [Du et al., 2024]	73.22	74.53	70.95	73.14	60.14	64.95	50.31	53.12	45.87	49.14	45.80	47.87	31.25	32.94	31.03	34.36	59.97	61.07	52.02	53.33	52.06	54.45
MuSe-Net	66.07	67.02	58.49	59.65	58.94	60.14	54.85	56.12	44.31	45.82	49.81	51.26	49.42	50.87	29.34	31.03	55.02	56.36	59.97	61.05	52.62	53.93
WeatherPrompt [Wen et al., 2025]	76.72	75.51	68.49	68.87	71.77	71.20	59.95	60.62	58.24	58.83	64.36	66.27	58.49	58.89	40.42	55.75	61.57	71.70	65.19	67.00	62.52	65.46
SKYPART (Ours)	97.21	98.10	96.27	97.59	96.06	97.53	95.33	97.05	94.71	96.75	90.44	93.85	95.17	96.94	92.06	94.50	93.34	95.85	96.54	97.80	94.71	96.60
Satellite \rightarrow Drone																						
Zheng et al. [Zheng et al., 2020]	70.20	57.98	63.77	46.90	68.72	50.85	61.72	39.70	62.10	32.75	71.70	40.39	59.72	37.55	45.49	25.28	52.11	43.40	56.62	45.31	61.21	42.01
IBN-Net	73.68	62.91	67.41	55.75	72.30	56.44	64.07	47.69	66.98	39.54	71.10	47.32	68.46	45.95	54.72	31.53	65.64	53.77	73.48	57.03	67.79	49.79
Sample4Geo [Deuser et al., 2023]	87.50	79.57	83.75	71.14	42.50	25.24	40.00	21.59	38.75	23.22	30.00	10.58	26.25	16.44	56.25	29.75	58.75	30.38	83.75	69.66	54.75	37.76
Safe-Net [Lin et al., 2025]	88.31	80.35	81.33	68.60	40.21	41.04	36.43	37.50	33.12	35.45	24.78	27.65	41.12	32.31	53.88	27.01	54.19	57.82	79.36	57.09	53.27	46.48
CCR [Du et al., 2024]	90.59	80.45	82.99	70.62	43.39	45.90	39.81	40.88	42.63	39.46	29.32	30.65	25.89	26.94	26.01	30.40	58.01	59.13	83.09	61.05	52.17	48.55
MuSe-Net	76.56	66.02	72.19	57.87	72.19	58.11	68.38	51.22	66.56	42.25	69.06	46.80	69.38	47.79	53.75	27.94	70.00	52.67	76.25	60.74	69.43	51.14
WeatherPrompt [Wen et al., 2025]	90.61	81.24	86.14	71.15	83.94	73.80	71.03	60.19	84.41	58.49	79.16	64.93	77.28	60.15	56.75	47.85	81.65	74.04	80.30	69.38	79.13	66.12
SKYPART (Ours)	98.75	98.24	98.75	97.56	98.75	97.52	98.75	96.94	98.75	96.17	98.75	92.11	98.75	96.72	98.75	93.79	98.75	95.90	98.75	97.21	98.75	96.22

A3.5 Zero-shot Cross-Dataset Transfer

Table 17 shows strong transfer under this protocol: SKYPART leads all $D \rightarrow S$ columns; on $S \rightarrow D$, DAC/MEAN slightly edge R@1 at 200 m and MCFA retains the strongest AP at higher altitudes, so the cross-dataset picture is mixed on $S \rightarrow D$. The point is that SKYPART attains non-trivial transfer on the primary $D \rightarrow S$ direction, supporting geographically meaningful structure beyond pure texture memorization.

A3.6 Additional Pareto Analysis

The picture that emerges is that SKYPART sits on the Pareto frontier in the accuracy–compute plane (Fig. 5), matching or exceeding the ConvNeXt-B baselines on every benchmark we test at a fraction of their parameter and compute budget. The per-altitude breakdown in Table 1 sharpens that observation: prior methods show a noticeable accuracy gap between the highest and lowest flight altitudes, while SKYPART narrows that gap and gains most at the lowest altitude, where partial facades dominate the field of view and a global descriptor has the least to work with. The qualitative evidence in Fig. 2 is consistent with the same picture: the same prototype fires on corresponding regions across the drone/satellite gap, even when the drone view is corrupted by weather. Taken together these observations are consistent with the framing we set: the representation that wins is one

Table 15: **Full WeatherPrompt robustness on University-1652**. Per-condition R@1/AP (%) for both D→S and S→D. Baselines are reported from WeatherPrompt [Wen et al., 2025]; SKYPART is evaluated under the same corruption pipeline at 392×392. This is the detailed University-1652 version summarized in Table 3. **Red**: best; **blue**: second.

Method	Clean		Fog		Rain		Snow		F+R		F+S		R+S		Dark		Over-exp		Wind		Mean	
	R@1	AP	R@1	AP	R@1	AP	R@1	AP	R@1	AP	R@1	AP	R@1	AP	R@1	AP	R@1	AP	R@1	AP	R@1	AP
Drone → Satellite																						
Zheng et al. [Zheng et al., 2020]	67.83	71.74	60.97	65.23	60.29	64.61	55.58	60.09	54.75	59.40	44.85	49.78	57.61	62.03	39.70	44.65	51.85	56.75	58.28	62.83	55.17	59.71
ResNet-101	70.07	73.04	63.87	68.22	63.34	67.59	59.75	64.15	57.45	62.12	48.31	53.28	60.25	64.68	46.12	51.02	56.34	61.23	62.13	66.63	58.76	63.29
DenseNet121	69.48	73.26	64.25	68.47	63.47	67.64	59.29	63.70	59.68	64.13	50.41	55.20	60.21	64.57	48.57	53.41	54.04	58.88	60.74	65.14	59.01	63.44
Swin-T	69.27	73.18	66.46	70.52	65.44	69.60	61.79	66.23	63.96	68.21	56.44	61.07	62.68	67.02	50.27	55.18	55.46	60.29	63.81	68.17	61.56	65.95
IBN-Net	72.35	75.85	66.68	70.64	67.95	71.73	62.77	66.85	62.64	66.84	51.09	55.79	64.07	68.13	50.72	55.53	57.97	62.52	66.73	70.68	62.30	66.46
LPN [Wang et al., 2022]	74.33	77.60	69.31	72.95	67.96	71.72	64.90	68.85	64.51	68.52	54.16	58.73	65.38	69.29	53.68	58.10	60.90	65.27	66.46	70.35	64.16	68.14
Sample4Geo [Deuser et al., 2023]	92.70	93.85	88.70	90.55	62.44	66.17	52.76	57.24	52.70	56.77	19.79	23.16	38.19	42.33	46.34	49.91	75.77	78.90	81.54	87.34	61.10	64.32
Safe-Net [Lin et al., 2025]	86.98	88.85	82.12	86.10	67.13	68.90	60.50	63.01	54.80	58.73	32.12	39.77	25.83	26.40	41.10	44.13	69.87	71.15	74.32	76.58	59.48	62.36
CCR [Du et al., 2024]	92.54	93.78	85.57	87.13	67.46	68.82	55.16	59.14	63.11	60.97	27.74	31.48	23.06	46.85	51.10	54.19	75.90	79.16	81.31	87.22	62.30	66.87
MuSe-Net	94.48	77.83	69.47	73.24	70.55	74.14	65.72	69.70	65.59	69.64	54.69	59.24	66.64	70.55	53.85	58.49	61.05	65.51	69.45	73.22	65.15	69.16
WeatherPrompt [Wen et al., 2025]	82.78	85.18	81.46	84.03	80.34	83.11	77.60	80.67	78.75	81.69	73.38	76.94	78.41	81.40	67.22	71.06	74.20	77.63	77.26	80.27	77.14	80.20
SKYPART (Ours)	95.15	96.45	93.78	95.65	93.44	93.98	92.05	93.51	90.05	92.74	88.51	91.86	89.47	92.42	83.26	87.80	88.23	91.50	89.68	92.54	90.36	92.84
Satellite → Drone																						
Zheng et al. [Zheng et al., 2020]	83.45	67.94	79.60	61.12	77.60	59.73	73.18	55.07	75.89	54.45	70.76	43.26	74.75	56.44	69.47	39.25	72.18	51.91	76.46	57.59	75.33	54.68
ResNet-101	85.73	71.79	82.45	66.46	81.46	65.68	79.74	61.72	79.74	60.59	74.75	50.31	80.17	62.61	75.32	45.37	79.60	58.21	82.31	64.67	80.13	60.74
DenseNet121	83.74	70.34	82.31	66.32	81.17	65.23	78.60	60.33	79.46	61.66	74.61	51.14	78.46	61.68	74.47	47.88	74.32	55.26	78.32	61.63	78.55	60.15
Swin-T	80.74	68.94	81.03	67.46	81.17	66.39	78.46	61.33	79.17	64.65	74.89	56.57	78.89	63.49	75.61	48.43	76.60	56.57	78.74	64.45	78.53	61.83
IBN-Net	86.31	73.54	84.59	67.61	84.74	69.03	80.88	64.44	83.31	63.71	77.89	52.14	83.02	65.74	78.46	50.77	79.46	58.64	84.02	67.94	82.27	63.36
LPN [Wang et al., 2022]	87.02	75.19	86.16	71.34	83.88	69.49	82.88	65.39	84.59	66.28	79.60	55.19	84.17	66.26	82.88	52.05	81.03	62.24	84.14	67.35	83.64	65.08
Sample4Geo [Deuser et al., 2023]	95.29	91.42	93.87	87.46	73.04	50.27	76.18	47.58	71.18	44.53	52.21	16.21	64.48	32.38	77.03	45.89	91.58	77.04	93.30	81.42	78.82	57.42
Safe-Net [Lin et al., 2025]	91.22	86.06	90.04	85.43	71.12	68.56	73.26	45.62	68.23	41.78	49.32	34.72	61.07	29.86	73.15	43.08	88.54	74.65	90.02	78.21	75.69	58.80
CCR [Du et al., 2024]	95.15	91.80	90.93	80.62	81.83	73.89	69.92	65.41	76.92	70.53	50.89	31.64	61.11	32.21	64.80	46.28	86.01	71.23	92.67	76.55	77.02	64.02
MuSe-Net	88.02	75.10	87.87	69.85	87.73	71.12	83.74	66.52	85.02	67.78	80.88	54.26	84.88	67.75	80.74	53.01	81.60	62.09	86.31	70.03	84.68	65.75
WeatherPrompt [Wen et al., 2025]	89.16	81.80	88.73	80.58	88.16	79.87	87.59	77.25	88.45	78.20	86.73	73.23	88.59	78.14	86.59	65.20	85.31	73.25	87.88	76.33	87.72	76.39
SKYPART (Ours)	97.29	97.08	93.15	90.62	93.87	90.03	92.01	88.51	92.58	87.72	91.87	83.64	91.44	88.06	92.30	80.18	91.73	87.30	92.01	88.17	92.83	88.13

Table 16: **Full WeatherPrompt robustness on DenseUAV**. Per-condition R@1/AP (%) for both D→S and S→D under the same corruption pipeline. AP denotes mean average precision over queries. This is the detailed DenseUAV version summarized in Table 3. **Red**: best; **blue**: second.

Method	Clean		Fog		Rain		Snow		F+R		F+S		R+S		Dark		Over-exp		Wind		Mean	
	R@1	AP	R@1	AP	R@1	AP	R@1	AP	R@1	AP	R@1	AP	R@1	AP	R@1	AP	R@1	AP	R@1	AP	R@1	AP
Drone → Satellite																						
Sample4Geo	72.37	66.67	72.42	66.31	73.66	66.84	72.80	66.37	73.14	66.37	70.44	65.06	72.59	66.47	66.50	61.54	69.76	64.86	72.29	65.87	71.60	65.64
CCR	56.76	62.37	55.21	61.35	55.94	61.84	54.70	61.71	54.10	60.74	51.48	58.33	55.30	61.46	49.85	56.11	54.44	60.43	54.87	61.42	54.26	60.58
IBN-Net	41.70	44.63	40.63	43.40	41.57	44.32	40.37	43.36	41.91	43.43	37.24	40.13	41.14	43.88	34.96	38.25	38.78	41.41	41.53	44.36	39.98	42.72
Safe-Net	41.14	45.55	39.47	44.78	40.11	45.20	37.11	42.72	37.54	43.91	31.87	38.39	39.30	44.81	33.20	37.93	37.07	43.01	40.03	45.15	37.68	43.15
MuSe-Net	28.96	32.56	26.77	31.88	27.71	32.39	26.94	31.17	26.38	31.41	21.54	26.55	26.98	31.69	23.25	27.12	24.88	29.45	28.70	32.64	26.21	30.69
WeatherPrompt	26.25	30.68	24.15	29.45	26.68	30.71	24.28	28.84	25.35	29.29	20.72	25.06	25.10	29.44	20.08	24.39	22.48	27.16	25.78	30.41	24.09	28.54
Zheng '20	17.55	22.58	19.18	23.59	18.88	23.38	18.15	22.47	19.65	23.82	17.72	21.56	18.53	22.98	14.63	19.08	16.00	20.40	18.53	23.56	17.88	22.34
SKYPART (Ours)	91.25	92.10	90.13	91.26	91.38	91.88	90.35	91.37	89.79	90.71	87.69	88.99	91.12	91.58	84.64	86.07	90.18	91.20	91.76	92.29	89.83	90.75
Satellite → Drone																						
Sample4Geo	71.51	67.44	70.61	66.68	71.77	67.00	72.03	67.01	70.79	66.20	69.37	64.45	71.34	66.65	66.67	59.81	69.33	64.85	71.34	65.97	70.48	65.61
CCR	56.93	60.85	55.38	59.24	57.83	60.27	56.41	58.80	55.77	58.49	52.17	54.58	56.28	58.80	52.38	50.40	55.30	55.91	56.54	59.92	55.50	57.73
IBN-Net	39.12	42.83	37.79	41.16	40.67	42.84	39.64	41.91	38.44	40.79	35.35	37.22	39.68	42.15	33.42	35.22	37.02	38.56	39.60	42.14	38.07	40.48
Safe-Net	38.40	40.20	37.19	39.51	37.71	40.06	36.12	37.46	36.94	38.54	33.25	33.11	38.01	39.38	32.13	31.86	38.74	37.57	38.78	40.56	36.73	37.83
MuSe-Net	27.03	31.35	26.00	30.00	27.54	30.84	26.51	29.32	25.57	29.41	21.58	24.20	26.38	29.33	23.55	24.36	23.08	26.28	27.76	30.56	25.50	28.57
WeatherPrompt	25.57	29.69	23.64	27.57	24.41	28.49	23.12	26.70	22.82	26.70	19.61	22.43	22.87	27.02	20.33	21.67	21.32	24.54	25.01	28.77	22.87	26.36
Zheng et al. [Zheng et al., 2020]	18.02	20.99	17.76	21.14	17.03	20.78	18.10	20.59	18.23	21.12	17.07	18.68	18.49	20.85	14.67	16.66	16.00	17.67	19.22	21.46	17.46	19.99
SKYPART (Ours)	92.66	92.34	91.55	91.21	91.51	91.66	92.02	91.54	90.99	90.43	88.61	91.93	91.55	90.69	84.79	92.15	91.30					

Table 17: **Zero-shot cross-dataset transfer:** University-1652 \rightarrow SUES-200 per altitude. All methods are trained on University-1652 only and evaluated on SUES-200 test set with no fine-tuning. **D \rightarrow **S** uses the 200-satellite confusion gallery. Baselines are from [Hou et al., 2025] and the original publications. Shading and red/blue ranks follow Table 1. **Red**: best; **blue**: second-best.**

Method	Drone \rightarrow Satellite								Satellite \rightarrow Drone							
	150 m		200 m		250 m		300 m		150 m		200 m		250 m		300 m	
	R@1	AP	R@1	AP	R@1	AP	R@1	AP	R@1	AP	R@1	AP	R@1	AP	R@1	AP
LPN	32.85	40.10	43.80	50.67	49.75	56.55	54.10	60.73	32.50	26.60	40.00	35.10	46.50	41.88	53.50	48.47
MCCG	57.62	62.80	66.83	71.60	74.25	78.35	82.55	85.27	61.25	53.51	82.50	67.06	81.25	74.99	87.50	80.20
Sample4Geo	74.70	78.47	81.28	84.40	86.88	89.28	89.28	91.24	82.50	76.20	85.00	82.93	92.50	87.77	92.50	88.38
DAC [Xia et al., 2024]	76.65	80.56	86.45	89.00	92.95	94.18	94.53	95.45	87.50	79.87	96.25	88.98	95.00	92.81	96.25	94.00
MEAN [Chen et al., 2025]	81.73	87.72	89.05	91.00	92.13	93.60	94.63	95.76	91.25	81.50	96.25	89.55	95.00	92.36	96.25	94.32
CAMP	76.53	80.47	87.18	89.60	93.75	95.04	96.40	97.18	88.75	78.17	95.00	88.31	95.00	91.85	96.25	93.43
MCFA	82.38	85.28	90.70	92.21	94.38	95.24	95.30	96.00	92.50	85.22	95.00	91.46	95.00	93.46	97.50	94.93
SKYPART (Ours)	85.68	87.96	92.23	93.64	94.43	95.55	96.43	97.45	93.75	89.36	95.50	90.96	96.25	92.74	97.50	94.61

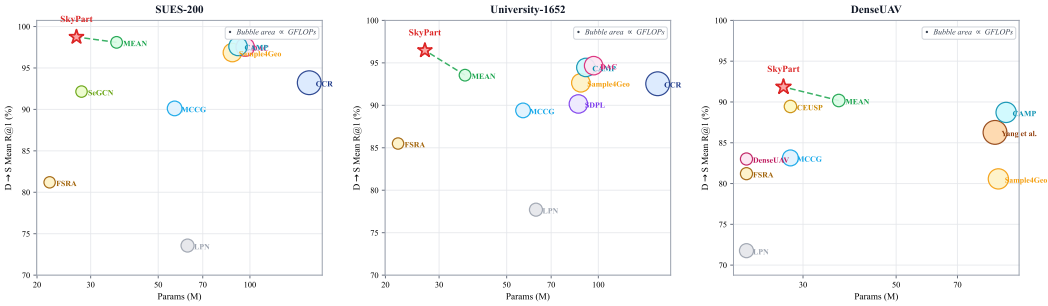


Figure 5: **Pareto efficiency across two benchmarks (D \rightarrow **S)**. R@1 vs. model size (params); bubble area \propto GFLOPs. SKYPART (blue star) is Pareto-optimal on both SUES-200 (left) and University-1652 (right), using fewer parameters and substantially lower compute than every baseline. Single-pass 448 \times 448; no re-ranking, no TTA.**

A4.2 Limitations and Broader Impact

Our train/test splits share a geographic region; cross-city or cross-continent generalization is untested beyond the University-1652 \rightarrow SUES-200 zero-shot experiment in Appendix A3.5. On that transfer, SKYPART leads all D \rightarrow S cells but trails MCFA and CAMP on several S \rightarrow D cells. Two factors likely contribute: prototypes trained on University-1652’s building-dense scenes do not fire cleanly on SUES-200’s road- and vegetation-heavy tiles, and the mean-FiLM fallback discards the altitude-band prior that normally separates low-altitude facades from high-altitude footprints.

The prototype bank capacity $K_{\max}=12$ is fixed; the salience gate handles per-image adaptivity within that ceiling but does not adjust it. Prototype assignments are label-equivariant—positives in the patch-NCE are pairs assigned to the same prototype in both views, not a fixed global index—so the loss stays well-defined when a prototype’s role drifts, but individual indices do not carry stable human-interpretable names. Removing the diversity regularizer \mathcal{L}_{div} produces collapsed prototypes within roughly 15 epochs. Rotation augmentation is DenseUAV-only; at continuous angles between the four 90 $^\circ$ training anchors the model relies on learned invariance, and smoothness is not guaranteed.

SKYPART is designed for emergency navigation in GPS-denied settings (search-and-rescue, inspection, disaster response). The same capability could enable unauthorized aerial surveillance. We recommend deployment be paired with privacy safeguards—anonimization, geographic access controls, and operator accountability—consistent with applicable law.

A4.3 What We Tried That Did Not Work

The take from the main paper is that explicit grouping complements global pooling rather than replacing it. Below are the directions we explored and dropped, with the specific failure mode in each case.



Figure 6: **Drone→Satellite top-5 retrieval.** Each row is a drone query at a given altitude (row label), followed by the SKYPART part-attention heat map and the 5 highest-ranked satellite matches. Amber = correct, blue = incorrect.

Geometric and transport priors. Polar warping [Shi et al., 2020] is the standard preprocessing for ground-panorama geometry, but on aerial tiles the reprojection is wrong and the train/test mismatch compounds it—accuracy dropped 8–12 pp across altitude bands. Sinkhorn OT matching over the two prototype banks was catastrophic under default hyperparameters; with careful tuning it reached parity with the contrastive baseline but never surpassed it. The failure mode is consistent: the transport cost matrix is ill-conditioned when drone and satellite patch tokens are correlated (they describe the same scene). Scene-graph GNNs with Sinkhorn matching and cross-view cross-attention both slowed convergence without adding signal that the symmetric alignment term was already providing.

Metric learning objectives. ArcFace (with and without sub-centers), Multi-Similarity, ghost-prototype absorbers, and triplet with batch-hard mining all underperformed Circle+proxy+InfoNCE+patch-NCE. The issue is geometric: a geolocation class is legitimately diffuse in embedding space because the same scene looks different across altitudes and weather conditions. Hard angular margins penalize exactly the spread the cross-view gap induces, so they suppress the signal rather than amplify it [Wang and Isola, 2020].

Reconstruction auxiliaries. Cross-view MAE [He et al., 2022] at the patch-token level helped on SUES-200 and hurt on DenseUAV and University-1652. A salience-masked variant—reconstructing only the patches the prototype bank attended to—did worse than random masking on all three. MAR (reconstructing the part aggregation rather than individual patch tokens) was the only reconstruction auxiliary that transferred consistently across datasets, because the reconstruction target is a layout summary rather than local texture.

Training dynamics. Warm-restart LR schedules, rotation augmentation on both views simultaneously, unfreezing more than 8 backbone blocks, and batch samplers that reduced optimizer steps per epoch below ~ 600 all regressed. The clearest case is rotation: it helps on DenseUAV (satellite tiles cropped at arbitrary basemap orientations) and costs 1.8 pp Mean R@1 on SUES-200 and University-1652 (canonically oriented pairs). Adding it universally destabilized the learned Kendall weights within the first 20 epochs.

Inference-time wrappers. Tent entropy minimization [Wang et al., 2021], multi-crop averaging, token merging, k-reciprocal re-ranking, and query expansion were not included in the reported

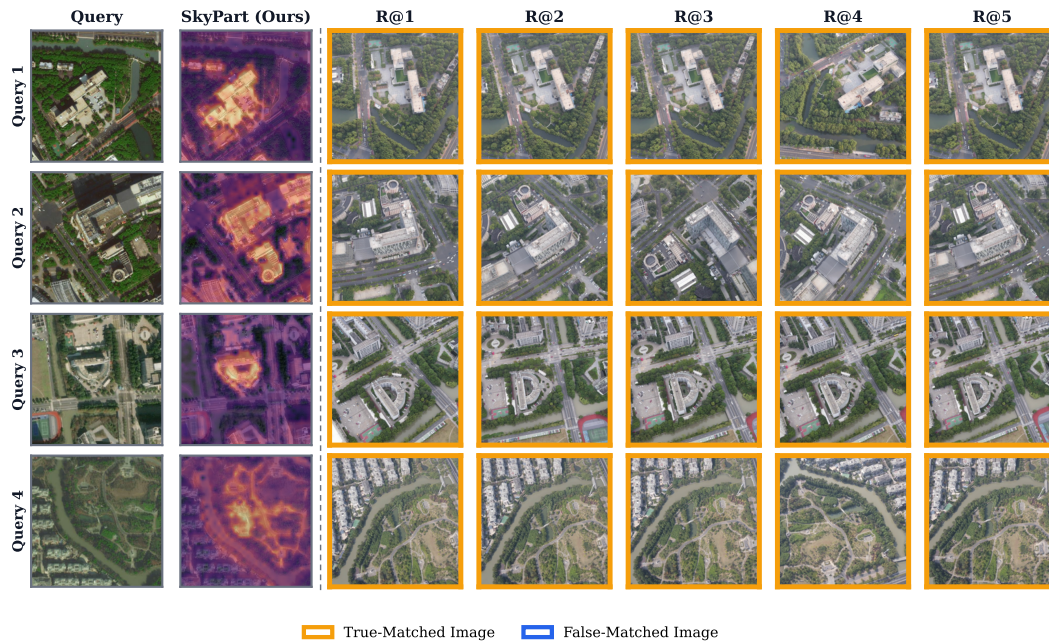


Figure 7: **Satellite**→**Drone top-5 retrieval**. Each row is a satellite query, its SKYPART part-attention heat map, and the top-5 drone images SKYPART retrieves across altitudes. Amber = correct, blue = incorrect.

numbers because they measure something different from the embedding itself. Each added 1–4 pp on at least one benchmark; a proper evaluation of how they compound with SKYPART is left for future work.